HHS Public Access

Author manuscript

Cell Rep. Author manuscript; available in PMC 2025 July 31.

Published in final edited form as:

Cell Rep. 2025 June 24; 44(6): 115758. doi:10.1016/j.celrep.2025.115758.

Cell-death pathways and tau-associated neuronal vulnerability in Alzheimer's disease

Gen Lin[1,6], **Sarah E. Chancellor**[2,6,7,*], **Taekyung Kwon**[2], **Maya E. Woodbury**[2], **Astrid Doering**[3], **Aicha Abdourahman**[2], **Rachel E. Bennett**[4], **Fan Liao**[2], **Timothy Pastika**[2], **Joseph Tamm**[2], **Nandini Romanul**[2], **Kiran Yanamandra**[2], **Miwei Hu**[5], **Karen Zhao**[2], **Matthew P. Frosch**[4], **Yelena Grinberg**[2], **Huan Li**[4], **Sudeshna Das**[4], **Tammy Dellovade**[2], **Eric H. Karran**[2], **Robert V. Talanian**[2], **Knut Biber**[3], **Alberto Serrano-Pozo**[4], **Janina S. Ried**[3], **Xavier Langlois**[2,*], **Bradley T. Hyman**[4,*]

[1]AbbVie Pte Ltd, North Buona Vista Road #19-01, Singapore 138588, Singapore

[2]AbbVie Inc., Cambridge Research Center, 200 Sidney Street, Cambridge, MA 02139, USA

[3]AbbVie Deutschland GmbH & Co. KG, Knollstraße, 67061 Ludwigshafen, Germany

[4]Department of Neurology, Harvard Medical School, MassGeneral Institute for Neurodegenerative Disease, Massachusetts General Hospital, Charlestown, MA 02129, USA

[5]Department of Neurology, MassGeneral Institute for Neurodegenerative Disease, Massachusetts General Hospital, Charlestown, MA 02129, USA

[6]These authors contributed equally

[7]Lead contact

SUMMARY

Neuronal loss is the ultimate driver of neural system dysfunction in Alzheimer's disease (AD). We used single-nucleus RNA sequencing and neuropathological phenotyping to elucidate

*Correspondence: sarah.chancellor@abbvie.com (S.E.C.), xavier.langlois@abbvie.com (X.L.), bhyman@mgh.harvard.edu (B.T.H.).

AUTHOR CONTRIBUTIONS

Conceptualization, G.L., T.K., M.E.W., R.E.B., Y.G., S.D., K.B., A.S.-P., X.L., and B.T.H.; methodology, G.L., S.E.C., T.K., M.E.W., A.W., F.L., J.T., K.Y., Y.G., S.D., K.B., A.S.-P., X.L., and B.T.H.; software, G.L., S.E.C., T.K., A.D., H.L., and S.D.; validation, S.E.C., T.K., T.P., N.R., K.Y., and Y.G.; formal analysis, G.L., S.E.C., T.K., A.W., H.L., and S.D.; investigation, S.E.C., T.K., M.E. W., A.A., T.P., J.T., N.R., K.Y., M.H., K.Z., S.D., M.P.F., and Y.G.; resources, G.L., T.K., M.E.W., M.P.F., J.S.R., X.L., and B.T.H.; data curation, G.L.; writing – original draft, G.L., S.E.C., and T.K.; writing – review & editing, G.L., S.E.C., T.K., M.E.W., A.W., R.E.B., F.L., K.Y., R.V.T., K.B., A.S.-P., J.S.R., X. L., and B.T.H.; visualization, G.L., S.E.C., and T.K.; supervision, T.K., M.E. W., R.E.B., F.L., K.Y., M.P.F., Y.G., S.D., T.D., E.H.K., R.V.T., K.B., A.S.-P., J.S.R., X.L., and B.T.H.; project administration, T.K., M.E.W., R.E.B., F.L., K. Y., M.P.F., Y.G., S.D., T.D., E.H.K., R.V.T., K.B., A.S.-P., J.S.R., X.L., and B. T.H.; funding acquisition, E.H.K., R.V.T., K.B., X.L., and B.T.H.

DECLARATION OF INTERESTS

G.L., S.E.C., T.K., M.E.W., A.D., A.A., F.L., T.P., J.T., N.R., K.Y., K.Z., Y.G., T. D., E.H.K., R.V.T., K.B., J.S.R., and X.L. were/are employees of AbbVie at the time of this work. The experimental design, execution, and financial support for this study were conducted and provided by AbbVie. AbbVie participated in the production and interpretation of data as well as the writing, review, and approval of the publication. B.T.H. has received research funding from AbbVie as part of a collaboration agreement with The General Hospital Corporation, d/b/a Massachusetts General Hospital. B.T.H. has a family member who works at Novartis and owns stock in Novartis; he serves on the scientific advisory board of Dewpoint and owns stock. He serves on a scientific advisory board or is a consultant for AbbVie, Avrobio, Axon, Biogen, BMS Cell Signaling, Genentech, Ionis, Novartis, Seer, Takeda, the US Department of Justice, Vigil, and Voyager. B.T.H.'s laboratory is supported by sponsored research agreements with AbbVie and F Prime and research grants from the National Institutes of Health, Cure Alzheimer's Fund, Tau Consortium, and the JPB Foundation. A.S.-P., H.L., S.D., M.W., M.P.F., and R.E.B. work on the AbbVie-Hyman Collaboration.

mechanisms of neurodegeneration in AD by identifying vulnerable neuronal populations and probing for their differentially expressed genes. Evidenced by transcriptomic analyses and quantitative tau immunoassays of human AD and non-AD brain tissue, we identified a neuronal population especially vulnerable to tau pathology. Multiplexed immunohistochemistry and *in situ* hybridization (*CBLN2* and *LINC00507*) validated the presence of the tau-vulnerable neuronal population and revealed a propensity of this population to bear tau pathology. Differentially expressed genes associated with phospho-tau pathology in these neurons revealed genes involved in apoptosis, cell-component dissociation (e.g., autophagosome maturation and actin filament depolymerization), and regulation of vesicle-mediated transport.

Graphical Abstract

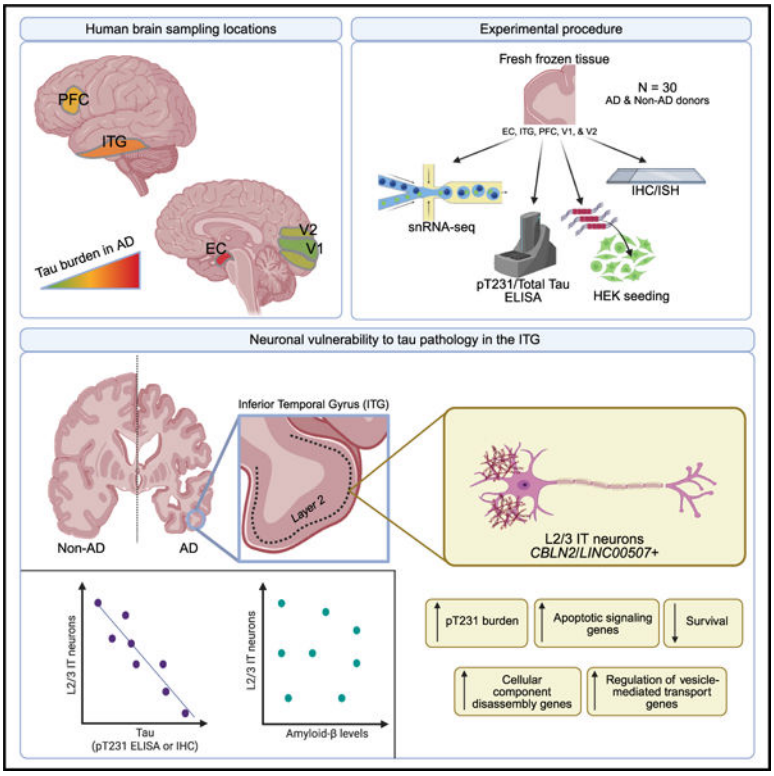

In brief

Lin et al. characterize a population of tau-vulnerable neurons in AD. Analysis of gene expression in these neurons reveals dysregulation in major coordinated programs including apoptosis, cell-component disassembly, and regulation of vesicle-mediated transport. These biological processes suggest avenues for therapeutic interventions preventing neuronal loss and degeneration in AD.

INTRODUCTION

Although neuronal loss is the ultimate mediator of neural system dysfunction in Alzheimer's disease (AD), its causes have been difficult to study. Neuronal loss correlates anatomically and regionally with the accumulation of tau pathology, which is readily measured

using histological and biochemical techniques.[1–6] The mechanistic link between tau accumulation and neuronal loss is still unknown. Understanding neuronal vulnerability and the relationship between tau pathology and neurodegeneration are critical gaps in our knowledge of AD pathogenesis.

For this purpose, many single-nucleus transcriptomic atlases have been produced using human AD brain tissues, which allow for a systematic investigation of cell-type-specific transcriptomic changes.[7–26] Most of these single-nucleus RNA sequencing (snRNA-seq) studies strive for larger sample size in a single brain region, which may not capture the full spectrum of progression of AD pathology across different neuronal subtypes and/or brain regions. Previous snRNA-seq studies conducted in AD brain revealed transcriptomic changes in excitatory neurons related to DNA damage response factors[7] and amyloid-β production and processing,[9] but it remains unknown whether such molecular changes are associated with tau pathology accumulated within the tissue.

Here, we hypothesized that excitatory neurons vulnerable to tau accumulation and neurodegeneration can be identified and transcriptionally characterized with snRNA-seq. We performed a large snRNA-seq study with >1.1 million nuclei derived from five brain regions selected to represent the stereotypical spatiotemporal progression of AD from 30 brain donors spanning the continuum of normal aging to severe AD[27–32] and tested for transcriptomic changes associated with local measures of tau pathology obtained within immediately adjacent samples. We identified characteristics of vulnerable neuronal populations and explored the cellular pathways that correlate with tau accumulation. We observe strong associations of phospho-tau (pTau) with genes identified by gene ontology (GO) terms as associated with apoptosis, cell-component disassembly (e.g., autophagosome maturation and actin filament depolymerization), and regulation of vesicle-mediated transport in this specific neuronal subpopulation.

RESULTS

Cell atlas mapping reveals region-specific neuronal subtypes

We designed the present study to directly investigate the transcriptional associations of neuronal subpopulations with tau pathology. We collected tissue samples from five brain regions that are stereotypically implicated in the spread of tau pathology in AD, namely the entorhinal cortex (EC), inferior temporal gyrus (ITG), prefrontal cortex (PFC), secondary visual cortex (V2), and primary visual cortex (V1),[27–32] from donors spanning from normal aging to severe AD on the neuropathological spectrum. To have high granularity of tau pathology represented in our sequencing samples, we selected an experimental cohort comprising 30 donors with varying levels of AD pathology based on global semi-quantitative measures of amyloid plaques (Thal phase), neuritic plaques (Consortium to Establish a Registry for Alzheimer's Disease [CERAD] score) and neurofibrillary tangles (NFTs; Braak stage). These donors presented with low (n = 6), intermediate (n = 5), and high (n = 12) AD neuropathological change burden, as well as donors classified as ''not AD'' (n = 7).[33]

To enrich for neurons, donor nuclei derived from all five brain regions were labeled with an anti-NeuN antibody and sorted via fluorescence-activated nuclei sorting (FANS) (STAR Methods and Figure 1A). After sequencing, we performed a label transfer from the BRAIN Initiative Cell Census Network (BICCN) reference dataset[34] and used two rounds of data integration to determine the threshold for removing doublets, low-quality cells, and nonneuronal cells (STAR Methods). A total of 1,111,850 neuronal nuclei (~35k per donor) passed quality controls and were annotated into 12 excitatory subtypes (662,834 nuclei) and 8 inhibitory subtypes (449,016 nuclei) (Figure 1B) after removal of doublets, low-quality cells, and non-neuronal cells. All inhibitory subtypes contained nuclei from all five brain regions (Figure 1C) and had highly homogeneous cell labels (>70%, Table 1).[34] We therefore annotated based on the majority label for inhibitory neurons (Table 1). For excitatory neurons, 4 out of the 12 subtypes were exclusive to one or two brain regions (Figure 1C), and we indicated the region specificity in their label (Table 1). For example, (V1/2) L4 *TRPC3* is exclusive to V1/V2, this cell type being primarily localized to layer 4 of the cortex in the BICCN[34] annotation (Figure 1C), and *TRPC3* is a primary marker gene, one of four listed in Table 1 for each neuronal subtype. Unlike (V1/2) L4 *TRPC3*,[35] the other three region-specific excitatory neurons ([V1/2] L4 *LINC02055*, [EC] L2/3 *PALMD*, and [ITG/PFC] L4 *RMST*) have not been described in previous studies to our knowledge. Using our annotated dataset as a reference, we performed a label transfer onto the Siletti et al. snRNA-seq dataset,[36] which includes many brain regions derived from non-pathological human brain samples. We confirmed that the region-specific neuronal subtypes in the present study show a similar region exclusivity across the current study and that by Siletti et al.[36] (STAR Methods and Figures S1A–S1C), demonstrating the consistency and reproducibility of the neuronal label annotations of the current dataset.

For downstream associations between snRNA-seq data and local pTau burden, tissue directly adjacent to that used for snRNA-seq was assessed for pTau with a pT231/Total Tau assay and for seeding competency through a fluorescence resonance energy transfer (FRET)-based seeding assay in HEK cells (hereafter HEK seeding assay; STAR Methods). pT231/Total Tau results paralleled the Braak stages of tau pathology burden across the five brain regions (EC, ITG, PFC, V2, and V1) (Figure 1D). By contrast, the HEK seeding assay was less sensitive, primarily revealing differences in Braak stages V and VI (Figure 1D).

Detection of a transcriptomic gradient in shared neuronal subtypes across brain regions

Next, we asked whether there is a broad transcriptomic signature of the EC-V1 axis and, if so, what are its molecular underpinnings. To address this question, we used a pseudobulk approach (STAR Methods) to examine transcriptomic differences in all AD and non-AD donors. For the analysis, we subset the 15 neuronal subtypes that are present across all brain regions: L2/3 intratelencephalic (IT), L4 IT, L5 IT, L6 IT, L6 cortico-thalamic (CT), L5/6 near-projecting glutamatergic neuron (NP), L6 *CAR3* IT, L6b, *LAMP5*, *LAMP5 LHX6*, *PVALB*, *SNCG*, *SST*, Chandelier, and *VIP* neurons (Figures 1C, S1D, and S1E; Table 1). We performed pairwise comparisons for each neuronal subtype between each region, with each individual region being compared to all other brain regions for a total of ten pairwise comparisons per neuron subtype. We identified more than 2,000 differentially expressed genes (DEGs) that were region specific (ranging from 2,352 to 5,499 genes depending on

the region; adjusted p value <0.05, absolute log(fold change) >0.5; Table S10). Applying principal-component analysis (PCA) to these region-defining genes revealed a continuum (Figure S2B) wherein the transcriptomic profile of neuronal subtypes appears to change along interconnected brain regions following the tau-vulnerable neural network defined by Braak from EC to V1 (Figures 1A and S2B).

To determine whether this transcriptomic gradient is driven by tau burden across the Braak-associated brain regions or simply represents regional differences existing in the normal brain, we repeated this analysis in the Siletti et al.[36] non-pathological, multi-region brain snRNA-seq dataset.[36] We identified a high number of common DEGs clustered in a similar pattern on the first principal component (Figures S2C and S2D; Table S11), confirming that this regional transcriptomic gradient is already present in the normal brain and is not inherently representative of changes induced by pTau pathology.

To understand the pathways underlying this brain-region-based transcriptomic continuum in our dataset, we performed a GO term enrichment analysis (STAR Methods). Notably, genes related to the extracellular matrix (e.g., glycosaminoglycan binding and heparin binding) decrease in expression from EC to V1, whereas genes involved in oxidoreductase activity increase in expression from EC to V1 (Figures S2E and S2F; Table S2). Thus, these regional analyses demonstrate the transcriptomic basis of the EC-V1 axis and nominate extracellular matrix and oxidative stress/antioxidant defense as pathways that might be involved in the selective vulnerability or resilience to either tau aggregation, tau propagation along neural networks, and/or tau-induced neurodegeneration.

Changes in regional and neuronal subtype gene expression with disease progression

Having established that there are multiple neuronal subtypes that exhibit a transcriptomic gradient along the EC-V1 axis in the normal aged brain, we next asked how tau pathology impacts gene expression in the various neuronal subtypes by first exploring the transcriptional phenotypes of global patterns of AD pathology through Braak stage.

We first identified DEGs associated with increasing Braak stages within each of the 15 neuronal subtypes represented in all five brain regions by using a similar pseudobulk approach. By regressing the gene expression of each neuronal subtype against Braak stage and brain region with sex as a covariate (STAR Methods), we detected a total of 9,714 unique genes that are associated with Braak stage (e.g., differential expression with increasing Braak stages) (Figure S2A). RNA integrity number (RIN) and postmortem interval (PMI) (Table S1) were not included as covariates to avoid overfitting of the regression model (STAR Methods). There were very few DEGs associated with either RIN or PMI in any brain region when compared to Braak stage, except for the PFC (STAR Methods and Table S9). The highest number of DEGs (total number of DEGs/total number of analyzed genes) were found in L2/3 IT excitatory neurons (ITG = 3,091, V2 = 3,441, and V1 = 2,934) followed by L5 IT excitatory neurons (ITG = 633, V2 = 1,343, and V1 = 3,556) (Figure S2A and Table S3), suggesting that they are the most affected by tau toxicity. Regionally, the ITG contained 10 out of the 15 neuronal subtypes showing >100 DEGs (6,580 total DEGs; Figure S2A and Table S3) with V2 and V1 containing 7 and 5, respectively. Notably, we detected fewer DEGs in the EC and PFC, which may be partly

explained by the fact that these two regions contained the lowest number of donor samples analyzed in this study (EC, 21 samples; PFC, 26 samples; Figure S2A and Table S1). In addition, both the EC and PFC contained region-specific neuronal subtypes that were not part of this analysis (Table 1).

Next, we investigated the intersection between these Braak-associated DEGs and the regional transcriptomic gradient described in the prior section. Multidimensional scaling (MDS; STAR Methods) on the 9,714 Braak-associated DEGs revealed that Braak-associated DEGs in both excitatory and inhibitory neurons segregate by brain region, with PFC, ITG, and V1/V2 neurons clustering separately (Figure 2A). Hierarchical clustering demonstrated consistent findings (Figures S3A and 2A). These data indicate that the gene-expression changes associated with AD progression as measured by Braak stages are not uniform across regions, generally following the patterns of spreading pTau pathology in AD.

To understand the pathways underlying Braak-associated DEGs, we performed a systematic differential gene-expression analysis comparing V2 (a Braak VI-defining region, thus relatively resilient to pTau) vs. ITG (a Braak III-defining region, therefore highly vulnerable to tau) followed by gene set enrichment analysis (GSEA; STAR Methods, Figure 2B, and Table S3). Notably, this analysis showed that genes associated with glutamate receptor signaling and response to acetylcholine are downregulated in V2 vs. ITG with increasing Braak stages, suggesting that pTau accumulation drives abnormal neuronal neurotransmission (Figures 2B, S3B, and S3C; Table S3). By contrast, mitochondrial electron transport chain genes and translation-associated genes are upregulated in V2 vs. ITG with increasing Braak stages (Figures 2B, S3B, and S3C), potentially demonstrating the negative metabolic and translational effects of high pTau burden.

Lastly, we looked deeper within the ITG, since it is the region with most neuron subtypes impacted by transcriptional differences and the region with the highest number of DEGs with increasing Braak stages (Figure S2A). Specifically, we investigated the gene-expression changes associated with Braak stage in each of the neuronal subtypes present in this region. A pairwise correlation heatmap of all Braak-associated fold changes of the 5,409 unique genes detected in the ITG, followed by hierarchical clustering, revealed that gene-expression changes in inhibitory neurons significantly differ from those of excitatory neurons (Figure 2C and Table 1). We performed GSEA to understand the pathways involved in the different Braak-stage-associated fold changes between the ITG inhibitory and excitatory neurons and detected 306 significant pathways (297 upregulated and 9 downregulated) (Figure 2D). Examination of the pathways and fold changes indicate that ITG excitatory neurons show a stronger increase in genes related to translation, exocytosis, apoptosis, and response to cytokine-related genes relative to ITG inhibitory neurons (Figure 2D and Table S3). However, ITG excitatory neurons also show a decrease in genes related to axon guidance, chemotaxis, and cell-junction assembly compared to ITG inhibitory neurons (Figure 2D and Table S3).

Transcriptomic and *in situ* identification of tau-vulnerable neurons in layer 2

After identifying the ITG as a locus of Braak-associated transcriptional shifts, we sought to determine whether there are proportional changes in any of the neuronal subtypes in

relationship with pathologic tau accumulation by stratifying pTau burden by pT231 levels. We hypothesized that a tau-vulnerable neuronal subtype would exhibit a negative correlation between its abundance and tau burden, whereas a tau-resilient neuronal subtype would not correlate with tau burden or even correlate positively. Further, we hypothesized that stratifying pTau burden by local pT231 levels (measured via ELISA in samples immediately adjacent to those used for snRNA-seq; STAR Methods) would allow for a more nuanced examination of the cell abundance and transcriptional shifts induced by pTau in the sequenced tissue than would Braak stage, which cannot account for or predict pTau burden on a micrometer scale.

We tested whether the proportion of neuronal subtypes is associated with local pT231 levels across all brain regions, while accounting for confounding variables such as sex, age, and RIN, using scCODA[39] (STAR Methods). With these strict criteria, we detected a significant negative association between the abundance of the L2/3 IT neuronal subtype in the ITG and local pT231 levels measured by both pT231/Total Tau ELISA (Figures 3A, 3B, and S1E)[39] and AT180 immunoreactivity (Figures S4D and S4E; STAR Methods), whereas the abundance of V1/2 L4 *LINC02055* neurons in V1 was positively associated with local pT231 levels (Figure S4A). We detected no such associations in the ITG when using Braak stage as a proxy for global tau burden, supporting a direct effect of nearby pTau rather than an effect of the neurodegenerative process (Figures S4B, S4C, and S1D).

To investigate the L2/3 IT neuron population in an anatomic context and better understand its spatial relationship with tau pathology, we performed histological validation through fluorescent *in situ* hybridization (FISH) for two marker genes of L2/3 IT neurons (*CBLN2* and *LINC00507*; Table 1), combined with immunohistochemistry (IHC) with anti-NeuN (neuron marker) and anti-AT180 (pT231 tau) antibodies in ITG cryosections adjacent to those used for snRNA-seq from all suitable donors ($n = 28$; Figures 3C and S5A; STAR Methods). Quantification of confocal imaging revealed a significant negative correlation between the relative abundance of the L2/3 IT neurons (Figure S5B; $NeuN^+$, $CBLN2^+$, and $LINC00507^+$ nuclei, STAR Methods) and the integrated intensity of AT180 immunoreactivity (Figures 3C and 3D; STAR Methods)), in line with the transcriptomic-biochemical association (Figure 3B).

Isocortical NFTs are known to accumulate following a laminar distribution with predominant involvement of layers 2 and 5.[30,41] Therefore, we investigated whether the decreasing proportion of transcriptomically defined L2/3 IT neurons observed with increasing pT231 levels is a result of pTau within L2/3 IT neurons. We compared the likelihood of AT180 positivity within the cell bodies of $CBLN2^+$ and $LINC00507^+$ neurons vs. all other neurons. L2/3 IT neurons had a significantly higher likelihood of cell-body AT180 positivity (Figure 3E) and had a significantly higher pT231 burden compared to the rest of the neurons in the same tissue section (Figure 3F). In summary, our snRNA-seq and pT231/Total Tau ELISA modeling results, combined with these FISH/IHC findings, support the idea that the transcriptomically defined L2/3 IT neuronal subtype has a selective vulnerability to both contain pTau and degenerate.

Although *CBLN2* and *LINC00507* have been proposed as marker genes for L2/3 IT neurons by the BICCN[34] annotation, we noted that FISH/IHC results did not demonstrate an obvious upper-layer localization of *CBLN2*/*LINC00507*-expressing nuclei. Indeed, there are mixed reports of the cortical layer expression phenotypes of *CBLN2* and *LINC00507*.[42,43] Since our FISH/IHC imaging region of interest was not suitable for a systematic, cortical-layer-based analysis, we decided to map the distribution of our L2/3 IT neurons in a published spatial transcriptomics study by Chen et al.,[40] who used the Visium 10× Genomics platform in the medial temporal gyrus of three AD and control donors.[40] We first performed a label transfer onto the Chen et al.[40] dataset to label their neurons with our cell-type annotation (STAR Methods). We found that the majority of the L2/3 IT-assigned spots were localized to the upper layers of both AD and control cortices (Figures 4G and S6A).[44–46] We then separately mapped the expression of *CBLN2* and *LINC00507*. *CBLN2* was expressed ubiquitously at generally high levels across all cortical layers with a specific predilection for layers 2 and 5 in most of the six donors analyzed, whereas *LINC00507* had very low expression overall but was primarily localized to the upper layers of the cortex (Figures 4G and S6B). We therefore concluded that *LINC00507* is more specific for L2/3 IT neurons than *CBLN2* (Figure S7A and Table 1) but that the high sensitivity of *in situ* hybridization with RNAScope technology (ACDBio) for low-abundance mRNAs[47] explains why our FISH/IHC highlighted *LINC00507*-expressing neurons throughout the cortical layers.

Transcriptomic profiling of L2/3 IT tau-vulnerable neurons with local pTau

Having established that the transcriptomic subcluster of L2/3 IT excitatory neurons predominately reside in layer 2 of the cortex, that they decrease in abundance with increased local pTau burden, and that they are more likely to bear pTau than the other neurons, we characterized their transcriptomic profile to ascertain potential molecular underpinnings of their selective vulnerability. To this end, we regressed the gene expression of ITG L2/3 IT neurons against pT231 levels. A total of 1,233 genes were significantly associated with pTau (q value < 0.05, 641 genes positively and 592 genes negatively, Figure 4A and Table S4). GO term enrichment analyses of the positively associated significant genes demonstrated an enrichment for terms related to apoptotic signaling (Figure 4E), cellular component disassembly, and regulation of vesicle-mediated transport (note that other pathways, including regulation of cellular pH, were also observed) (Figures 4B and S7B). The cellular disassembly gene set (Figure 4B) demonstrated engaged subpathways such as autophagosome maturation and actin filament depolymerization (Figure S7E and Table S5). Importantly, these GO term associations were not detected in other neuron subtypes in the ITG (Figure S7C), suggesting they are specific to L2/3 IT neurons and that, therefore, these pathways are relevant to tau aggregation and tau-induced neurodegeneration.

In exploratory analyses, we asked whether this same population of cells showed altered expression of other cell-death pathway-related terms (Reactome[48] and additional GO term pathways). The intrinsic apoptotic signaling in response to ER stress pathway, and other closely related apoptosis pathways, was also statistically significant (Figure S9 and Table S5). The odds ratio (OR) of neuronal apoptotic process (OR = 2.1, p = 0.007) was comparable to that of lymphocyte apoptotic processes (OR = 2.64, p = 0.052), although with stronger statistical significance. Regulation of necroptotic cell death, *RIPK1*-mediated

necrosis, and regulated necrosis had an OR > 1; however, all terms were assigned a non-significant *p* value ($p = 0.08$; Figure S9 and Table S5). Of the key genes in this pathway (e.g., *RIPK1*, *RIPK3*, and *MLKL*), only *RIPK1* was detected as differentially expressed in L2/3 IT ITG neurons, and it was significantly downregulated (Table S4). Therefore, in terms of established cell-death mechanisms, apoptosis-related pathways appear to be most implicated by these data. Moreover, we asked whether amyloid-β burden was related to the three highest ranked GO terms–apoptosis, cell disassembly, and regulation of vesicle-mediated transport–and found that the average effects of pTau pathology more heavily drive activation of these pathways than β-amyloid, as measured by 3D6 immunoreactivity in cryosections adjacent to those used for snRNA-seq (Figures S10A and S10B; STAR Methods). Further, we examined whether amyloid-β pathology held the same significant negative association between the abundance of the L2/3 IT neuronal subtype in the ITG as does pT231 and found no change between any neuronal subtype in the ITG and 3D6 immunoreactivity (Figure S10C).

In silico validation of L2/3 IT neurons as a tau-vulnerable subpopulation

To validate the identification of transcriptomically defined L2/3 IT neuron subtype as tau-vulnerable neurons, we leveraged a single-cell transcriptomics dataset of tangle-bearing ($AT8^+$) and tangle-free ($AT8^-$) neurons isolated from the PFC of late-stage AD donors conducted by Otero-Garcia et al.[12] After the label transfer of our snRNA-seq dataset onto the Otero-Garcia et al. dataset (STAR Methods and Table S6), we observed that the most $AT8^+$ neurons mapped to our L2/3 IT neurons, whereas other neuronal subtypes such as *LAMP5*, L4 IT, and *PVALB* were absent in the $AT8^+$ neuronal fraction (Figure 4C). We next compared the gene-expression profile of L2/3 IT neurons in the dataset of Otero-Garcia et al.[12] and our dataset. We compared the pT231-associated gene fold changes from our L2/3 IT ITG neurons to the $AT8^+$ vs. $AT8^-$ fold changes in the Otero-Garcia et al.[12] L2/3 IT subpopulation and observed a positive correlation (Spearman's rank correlation coefficient = 0.56, $p < 2.2e{-}16$; Figure 4D and Table S6). Noteworthy, the cross-study correlation was stronger for the L2/3 IT neurons than for the (ITG/PFC) L4 *RMST*, L4 IT, L5 IT, L6 IT, *PVALB*, *SST*, and *VIP* neuronal subtypes (Figure S7D), further supporting our conclusion that L2/3 IT neurons are the most vulnerable to tau-induced degeneration (Figures 3A, 3B, and 3D) and bear pTau (Figures 3E and 3F).

We also compared our findings with those from other prior transcriptomic studies identifying tau-vulnerable neuronal subpopulations. Studies have detected vulnerability in *WFS1*-expressing[49,50] and *DEK*-expressing[51] EC neurons, *JADE1*-expressing neurons (in primary tauopathy[52]), and *BAG3*-expressing excitatory neurons.[53] However, none of these four genes were enriched in L2/3 IT neurons in the ITG (Table S4). Leng et al.[17] identified two tau-vulnerable neuronal populations of interest ($RORB^+$ and $TLL1^+$) in the EC, but not in superior frontal gyrus.[17] We were unable to detect a tau-vulnerable neuronal population in the EC, likely due to our limited number of EC samples (Table S1) and the relatively large loss of vulnerable neurons in layer 2 of the EC even in preclinical stages of disease.[41] In 2023, Mathys et al.[7] primarily focused on the vulnerability of two inhibitory subtypes (SST^+ and $RELN/LAMP5^+$) and linked their depletion to cognitive deficits in AD, but they also identified an excitatory population (Exc L2–3 CBLN2 LINC02306)

whose cellular abundance correlated with global AD pathology, various cognitive symptoms, and semi-quantitative measures of tau pathology.[7] Notably, this neuronal population did not have strong cellular abundance associations with diffuse plaque burden and did not correlate with overall amyloid level,[7] similar to the lack of association we observe between amyloid-β and the abundance of L2/3 IT ITG neurons (Figure S10C). When comparing the $\log_2$(fold change) of the differential gene expression of our L2/3 IT ITG neurons to the fold changes of a subset of neuronal populations from Mathys et al.,[7] we identified a significant overlap in gene expression with their Exc L2–3 CBLN2 LINC02306 and Exc L3–4 RORB CUX2 subpopulations (Figure S8). These similarities in gene expression across excitatory neuronal subtypes were most prominent in gene sets associated with global AD pathology and tau-related scores in Mathys et al.[7] (Figure S8). Using the same semi-quantitative measures of tau pathology in a multi-brain-region snRNA-seq study of AD, in 2024, Mathys et al.[54] found a negative association between subtypes of entorhinal neocortical L2/3 neurons (L2 $RELN^+$ from the lateral EC, L3 $RELN^+$, L5, and L2/3 $TOX3^+$ $TTC6^+$ neurons) and high NFT levels. Further, they found that with lower numbers of these populations of neurons, donors performed worse on cognitive tasks. Particularly examining Exc L2–3 CBLN2 LINC02306 neurons, they found associations between the subtype's gene expression and a number of cognitive performance measurements but found only one correlation between worsening perceptual orientation when examining Exc L2–3 CBLN2 LINC02306's cellular abundance.[54] A reduction in Exc L2–3 CBLN2 LINC02306 neuron abundance was only observed in late AD and was associated with NFT and diffuse plaque load.[54] In analyses of transcriptomic correlations of Exc L2–3 CBLN2 LINC02306 gene expression with pathological scores, they found association with global AD pathology and semi-quantitative measures of tau along with a lower, yet significant, correlation with overall amyloid level, largely mirroring the findings in Mathys et al.[7] Lastly, Gabitto et al.[10] have reported a decrease in the number of L2/3 IT neurons (also based on the BICCN[34] annotation) with an increasing pathology score modeled based on pTau, amyloid-β, and other pathological protein markers derived from IHC of the temporal gyrus (Brodmann area 21) directly above the ITG (Brodmann area 20).[10]

Regarding comparisons of pathway enrichment, we detected several similarities and differences between the current study and others examining neuronal abnormalities and cell death in the context of pTau and amyloid-β pathology. A major pathway that emerged from our analysis is regulation of vesicle-mediated transport. Multiple lines of evidence implicate defects in vesicular transport in AD. Dysfunction of the retromer complex has been implicated in Down syndrome[55] and AD,[56] and it has been demonstrated that VPS26b deficiency occurs in vulnerable brain regions in AD.[57] Indeed, the DEG list derived from L2/3 IT ITG neurons has several significant VSP-family genes (Table S4). Regarding the detection of apoptosis as the major cell-death pathway implicated in this dataset (Figures 4B, 4E, and S7C), we detected differences in comparison to another study. In Balusu et al.,[58] an upregulation of *MEG3* and genes linked to necroptosis were found in H9-derived cortical neural progenitor cells in xenografted *App*-knockin mice. In the current study, only apoptosis-related terms were enriched in L2/3 IT ITG neurons, and *MEG3* was not differentially expressed (Figures 4B and S7C and S9; Tables S4 and S5). We compared the gene-expression profile of pT231-associated gene fold changes from L2/3 IT ITG neurons to

the gene fold changes of the xenografted neurons, which were found to bear pTau pathology as early as 6 months post transplantation,[58] and found a poor, yet significant, correlation ($r = 0.044$, $p = 2.281e{-}07$; Figure S11). To better understand any similarities between both datasets, we then compared the positive and negative pT231-associated gene fold changes from our ITG L2/3 IT neurons to positive and negative gene fold changes of the xenografted neurons, respectively, and found no clear associations (upregulated: OD = 1.06, $p = 0.45$; downregulated: OD = 1.05, $p = 0.67$; Table S7). This lack of association, in addition to the diverging cell-death pathways activated in L2/3 IT and grafted neurons, suggests that different pathological changes may underlie neurodegeneration in these two pTau-laden neuronal populations.

DISCUSSION

We approached the long-standing question of selective vulnerability in AD[1,3,30,59] by characterizing the transcriptome of neurons across five brain regions known to be affected sequentially in stereotypical AD of 30 donors spanning the normal aging-to-severe AD continuum and correlating the abundance of the transcriptomics-based neuronal subtypes and their gene expression with both global tau burden (Braak stage) and local pTau231 levels. We found that, of all transcriptomic excitatory and inhibitory neuronal subtypes identified, L2/3 IT excitatory neurons are the most vulnerable to loss and tau aggregation.

Compared to others, a strength of our study was the measurement of pT231 levels by ELISA in samples immediately adjacent to those used for snRNA-seq to better assess the impact of the local burden of pTau on neuronal gene expression. Indeed, we were unable to replicate the negative correlation between L2/3 IT neuronal abundance and pT231 levels when using the less quantitative measure of Braak stage (Figures S4B and S4C), which may partially explain the discrepancy in neuronal subtype abundance changes between our study and both Mathys et al. (2023[7] and 2024[54]) and Leng et al.[17] However, we were able to replicate the negative correlation between L2/3 IT neuronal abundance and pT231 levels using quantification of anti-AT180 (pT231) IHC staining from tissue sections derived from samples immediately adjacent to those used for snRNA-seq (STAR Methods; Figures S4D and S4E). Other snRNA-seq studies not focused on neuronal vulnerability have used pTau IHC readouts obtained from FFPE sections of the hemisphere contralateral to that used for snRNA-seq,[15,16] with one study specifically noting a discrepancy between Braak stage and IHC-based pTau burden.[16] Gazestani et al.[9] used pTau IHC in sections neighboring those used for sequencing but with a binary readout of presence or absence of pTau while analyzing for amyloid-β-vulnerable neuronal populations.[9] Gabitto et al.[10] used IHC from a tissue block neighboring that used for sequencing and developed a pathological scoring system with multiple readouts, which correlated with Braak stage, amyloid-β, and pTau immunoreactive area fractions.[10]

Gene sets known to be activated during apoptosis were clearly and specifically engaged by L2/3 IT neurons (Figures 4B, S7B, and S7C). Other cell-death pathways have been implicated in experimental models of AD,[60] including caspase-2, NLRP-mediated inflammasome expression, and necroptosis[60,61]; however, only apoptosis was found to be statistically significant as a cell-death pathway from the GO analysis of the L2/3 IT ITG

differential expression gene list (Figures 4B and S7C) in our analysis of human AD. We postulate that a cellular disassembly gene set (Figure 4B), also implicated by the analysis of GO terms, is similarly related to cell-death processes, as highly repeated GO names within the GO terms reveal subpathways such as autophagosome maturation and actin filament depolymerization (Figure S7E and Table S4). Taken together, we characterize a tau-vulnerable neuronal population with abnormalities in at least three major coordinated programs (apoptosis, cell component disassembly, and regulation of vesicle-mediated transport), suggesting avenues for therapeutic interventions to prevent neuronal cell loss and degeneration in AD.

Limitations of the study

Despite this large dataset, our analysis still may be underpowered to detect many effects, given the heterogeneity of sampling from the five different brain regions and multiple stages of disease that we examined. We also anticipate that additional pathways, cell-cell interaction targets, and neural-system-based changes may emerge from combining the data presented here with that from analogous snRNA studies of endothelial cells,[62] microglia,[11] and astrocytes[63] derived from the same underlying tissue samples. Data from each of these studies are publicly available. Further, unlike the Religious Orders Study and Memory and Aging Project (ROSMAP) cohort and subsequent AD snRNA-seq studies,[7,20,54,64,65] no testing regarding cognitive state, neither longitudinally nor cross-sectionally, was available for these donors, which limits the scope of our analysis to neuropathological associations with neuron subtype abundance and gene expression. Sex-based analyses were not performed due to limited sample size of male donors (Table S1) and female sex of HEK cells, which may limit the generalization of our findings. However, sex was controlled for as a confounding variable in statistical analyses (STAR Methods). Lastly, there was an effect of PMI on the differential expression of genes from the PFC (STAR Methods and Table S9), which may have affected the number of Braak-stage-associated detected DEGs in this brain region.

RESOURCE AVAILABILITY

Lead contact

Sarah E. Chancellor (sarah.chancellor@abbvie.com) is the lead contact for this study.

Materials availability

This study did not generate new unique reagents.

Data and code availability

- Raw sequencing data derived from human samples have been deposited at NCBI as BioProject: PRJNA1142727. Processed and analyzed sequencing data derived from human samples have been deposited in Zenodo: 13222113. This paper also analyzes existing publicly available data. The accession numbers for these datasets are listed in the key resources table. Reanalyzed sequencing data derived from human and mouse samples from publicly available data have been deposited in Zenodo: 13222113.

- All original code has been deposited in Zenodo and is publicly available at Zenodo: https://doi.org/10.5281/zenodo.13222113 as of the date of publication.
- Any additional information required to reanalyze the data reported in this paper is available from the lead contact upon request.

STAR★METHODS

Detailed methods are provided in the online version of this paper and include the following:

EXPERIMENTAL MODEL AND STUDY PARTICIPANT DETAILS

Human donor tissue: Donors ($N = 30$) were selected from the Neuropathology Core of the Massachusetts Alzheimer's Disease Research Center (ARDC), which obtained written informed consent per institutional policy. Fresh frozen human brain tissue was provided by the ADRC with approval from the Mass General Brigham IRB (1999P009556). Tissues were assessed by a neuropathologist for AD-related neuropathology burden according to NIA-AA guidelines[87] and included high pathology Braak V/VI donors ($n = 16$), intermediate pathology Braak III/IV donors ($n = 4$, and low pathology Braak 0-II donors ($n = 10$). For each donor, frozen postmortem cortical tissue was obtained from the following five brain regions when available: entorhinal cortex (EC, BA28, $n = 19$), inferior temporal gyrus (ITG, BA20, $n = 28$), prefrontal cortex (PFC, BA46, $n = 25$), secondary visual cortex (V2, BA18/19, $n = 27$), and primary visual cortex (V1, BA17, $n = 26$) (Table S1). All donor tissue from each region of interest was dissected into discrete samples for downstream analyses. All available information, including sex, age at death, Braak stage, postmortem interval, and comorbidities is disclosed for each donor in Table S1. Neither clinical and cognitive testing data nor information regarding gender, ancestry, race, socioeconomic status, or ethnicity was available.

Cell culture: Transduced human fetal embryonic epithelial kidney cells (HEK293T) with tau RD P301S-CFP and tau RD P301S-YFP constructs were cloned and obtained from ATCC (tau RD P301S FRET biosensor; RRID: CVCL_DA04). Cells were maintained in DMEM supplemented with 10% FBS and penicillin–streptomycin at 37C and 5% CO2 in a humidified atmosphere. Sex of cells were female. Cells were not authenticated. All cells used in this study were tested for mycoplasma contamination and found negative.

METHOD DETAILS

snRNA-seq: Nuclei isolation was performed as previously described with minor modifications.[15] Briefly, fresh frozen tissue was cryosectioned (approximately 40 sections at 40μm) and lysed in sucrose lysis buffer (10 mM Tris–HCl (pH 8.0); 320 mM sucrose; 5mM CaCl2; 3 μM $Mg(Ac)_2$; 0.1mM EDTA; 1mM dithiothreitol (DTT) and 0.1% Triton X-100). Lysates were filtered through a 70μm cell strainer. Nuclei were purified by ultracentrifugation (107,000 x *g* for 1.5 h at 4C) through a sucrose cushion (10mM Tris–HCl (pH 8.0); 1.8M sucrose; 3 μM $Mg(Ac)_2$; 0.1mM EDTA and 1mM DTT). Supernatants were removed and pellets were re-suspended in 2% BSA/PBS containing RNase inhibitor (0.2U/μL) (Roche). Nuclei were incubated with a fluorescently conjugated mouse anti-NeuN antibody (Alexa Fluor 647; Novus Biologicals, 1:3,000, RRID: AB_2927662) as a

neuronal marker and a mouse anti-Olig2 antibody (PE; Millipore Sigma, 1:250, RRID: AB_11205039) as an oligodendroglial marker.

Samples were kept on ice throughout the isolation and staining procedure. Nuclei were stained with Sytox blue (Thermo Fisher Scientific) and sorted on a BD FACSAria Fusion Flow Sorter (BD Biosciences). For each sample, we collected Sytox+, NeuN+, and Olig2^{-} nuclei. Single-nucleus cDNA libraries were constructed using the Chromium Single Cell 3' Reagent Kit V3 (10X Genomics). Samples were pooled and sequenced targeting at least 30k reads per cell on a NextSeq 2000 system (Illumina). As the samples were collected via cryosectioning, there is a possibility that fragmented nuclei were included in the nuclear isolation and FANS procedures. If this were the case, the fragmented nucleus would require adequate levels of transcripts to be included in our analyses as our computational pipelines exclude samples with 600 or fewer genes detected as detailed below (STAR Methods, Single nucleus data processing).

RNA integrity number (RIN) determination: Approximately 10–20mg of tissue from the visual cortex of each donor was homogenized using a Precellys CK14 Lysing Kit (Bertin) and RNA was extracted according to manufacturer's instructions with a MagMAX mirVana Total RNA Isolation Kit (Applied Biosciences). RIN was measured on with a 4200 TapeStation System (Agilent) to select high-quality tissue for snRNA-seq. RIN value was measured from 130 donors, for which 83 met the selected cutoff of RIN ≥5. Of 83 donors, 30 (Table S1) were selected based on the criteria listed above. Subsequently, RIN values were measured from all EC, ITG, PFC, V2 and V1 pieces used for snRNA-seq.

pT231/Total Tau ELISA: Protein extracts were prepared from 25mg of frozen tissue adjacent to that used for snRNA-seq. Approximately 40μm of tissue was collected for snRNA-seq, the following 40μm of tissue was collected for pT231/Total Tau ELISA, giving the maximal distance of samples used for sequencing to ELISA to be within an ~80μm range. Using dounce homogenization in 5 v/w of phosphate buffered saline (PBS) and centrifugation at 3,000 x *g* for 5 min at 4°C, the insoluble material was pelleted from each donor. Resulting supernatants were subjected to ELISA for Total Tau and tau phosphorylated at Threonine-231 (pT231) using a Phospho(Thr231)/Total Tau Kit (Meso Scale Diagnostics) according to the manufacturer's instructions.

HEK biosensor cell seeding assay: Tau bioactivity was measured as described previously using human embryonic kidney (HEK) cells expressing tau repeat domain with disease-associated P301S mutation fused to either CFP or YFP (ATCC).[88,89] HEK cells were cultured in Costar Black (Corning) clear bottom 96-well plates (previously coated with 50 μg/mL poly-D-lysine) for 14–18 h at 30,000 cells per well to reach 60% confluency. Human brain lysates with 1μg of total protein were mixed with 1% lipofectamine 2000 in OPTI-MEM and were treated to cells. After 48h of incubation, cells were trypsinized and fixed with 2% paraformaldehyde at room temperature. A MACSQuant VYB flow cytometer (Miltenyi) was used to measure mean FRET intensity and the percentage of FRET-positive cells per well. Multiplication of these values yielded the integrated FRET density (IFD) (Figure 1D and Table S1). Cells treated with lipofectamine alone were used as a negative control. In addition, AD and non-AD brain lysates were used as positive and negative

controls on each plate and used to normalize values for comparisons across all samples. All samples were analyzed in duplicates.

Human brain tissue sectioning and fixation for histology: Unfixed human brain tissue (3D6 IHC: all available brain regions, $n = 116$; FISH/IHC: only ITG, $n = 26$; Table S1) was stored at −80C until time of cryosectioning. Donor tissue was eliminated from the *in situ* analyses (FISH/IHC: 4 ITG donors eliminated; 3D6 IHC: 9 slides eliminated across all brain regions) due to poor tissue quality of cut slides. Tissue was adhered to cryostat chucks and allowed to acclimatize inside of a cryostat set to −17C for at least 1h. Tissue sections were cut at 10μm and placed onto chilled Superfrost Plus microscope slides (Fisher Scientific). Slides were produced using the same tissue blocks used for sequencing and pT231/Total Tau ELISA. Slides were placed for short-term storage at −80C until time of fixation. Slides were placed on a 60C slide warmer for 15min to ensure rapid tissue drying and tissue adherence to slides. Slides were allowed to cool at RT for 5min. Slides were placed in 10% neutral buffered formalin at RT for 1.5h. Slides were subsequently transferred for 2min each to baths of 50% EtOH, 70% EtOH, and 100% EtOH for tissue dehydration. Slides were then placed on a 60C slide warmer to dry fully for 30min and stored at RT.

Fluorescent multiplexed immunohistochemistry (IHC) and *in situ* hybridization (ISH): Fluorescent multiplexed FISH/IHC was performed using the RNAscope LS Multiplex Fluorescent Reagent Kit (ACDBio) and a BOND Polymer Refine Detection Kit (Leica) on a BOND-III automated staining system (Leica). Staining on human brain tissue with *CBLN2* (GenBank: NM_182511.4) and *LINC00507* (GenBank: NR_046392.1) probes (ACDBio) with mouse anti-AT180 (Thermo Fisher Scientific, 1:200, RRID: AB_223649) and rabbit anti-NeuN (Abcam, 1:150, RRID: AB_2927651) antibodies was conducted with custom protocols. Horseradish peroxidase (HRP)-conjugated anti-mouse or anti-rabbit secondary antibodies were used at a 1:2,000 dilution. All probes and antibodies were visualized with tyramide signal amplification (TSA) with Opal dyes at a dilution of 1:150 for antibodies or 1:100 for probes (Opal 480, 540, 570, and 690; Akoya Biosciences). DAPI (Thermo Fisher Scientific) was diluted to a 1:1,000 concentration and slides were incubated manually after removal from the autostainer for 10min. Slides were coverslipped manually with ProLong Gold Antifade mounting media (Thermo Fisher Scientific) and stored at 4C until imaging. All human brain tissue sections used for staining were produced and processed as described previously. Of the 30 donor samples, 4 samples were eliminated from quantification due to poor tissue quality (Table S1). Images were acquired with a Zeiss LSM 880 confocal laser scanning microscope using Zen Black software (Zeiss). A region of interest was defined at 10X magnification (Plan-Apochromat 10×/0.45 WD = 2.0 M27) for each tissue section using DAPI signal. Each region of interest was set at a fixed width (405.0μm) and included the full length of the cortex to visualize a full cortical column (Figure S5A). Each region of interest was tile scanned using a 63X oil objective (Plan-Apochromat 63×/1.4 Oil DIC UVVIS-IR) with 3 z-stacks taken with an optical slice thickness of 1.0μm. Maximum intensity projections of each tile scan were created in Zen Blue (Zeiss) and used for image analysis. Negative control images for both probes (Channel 1 and Channel 2) used for *in situ* hybridization were conducted using probes

for a bacterial gene (*DapB*, GenBank: EF191515.1; Figure S5C). *In situ* hybridization and imaging parameters were identical to those used for *CBLN2* and *LINC00507* experiments.

Immunohistochemistry (IHC) of amyloid-β pathology: IHC was performed using a BOND Polymer Refine Detection Kit (Leica) on a BOND-III automated staining system (Leica). Staining on human brain tissue with mouse anti-N-terminal amyloid-β antibody clone 3D6 antibody (AbbVie Inc., 2 μg/mL) was conducted with custom protocols. All human brain tissue sections used for staining were produced and processed as described previously. A total of 116 slides were produced from all available brain regions from the 30 donors. Nine slides (EC:4, ITG:1, PFC:2, V1:2) were eliminatedfrom quantification due to poor tissue quality (Table S1). Brightfield full slide scans were acquired using a Pannoramic 250 FLASH III scanner (3DHISTECH) with a 20X objective (Plan-Apochromat 20×/0.8).

Immunohistochemistry (IHC) of AT180 pathology: IHC was performed using a BOND Polymer Refine Detection Kit (Leica) on a BOND-III automated staining system (Leica). Staining on human brain tissue with mouse anti-AT180 (pT231) antibody (Thermo Fisher Scientific, 1:200, RRID: AB_223649) was conducted with custom protocols. All human brain tissue sections used for staining were produced and processed as described previously. Slides were produced from ITG tissue adjacent to that used for sequencing as available from the 30 donors. Three sections were eliminated from quantification due to poor tissue quality (Table S1). Brightfield full slide scans were acquired using a Pannoramic 250 FLASH III scanner (3DHISTECH) with a 20X objective (Plan-Apochromat 20×/0.8).

QUANTIFICATION AND STATISTICAL ANALYSIS

Processing of snRNA-seq reads and label transfer: CellRanger software (v.7.0.1; 10X Genomics) was used to map reads onto the reference human genome GRCh38. The ‘GRCh38-2020-A’ file set distributed by 10X Genomics was used as a transcriptome model. By default, this version of CellRanger includes intronic reads so we ran CellRanger with the default options. For each sample, we performed pre-processing in Seurat[82–86] using scTransform[80,81] (method = ‘‘glmGamPoi’’, variable.features.n = 4000), followed by PCA (20 PCs), and clustering (resolution = 0.2, algorithm = 3) to estimate contamination or doublet probability for each cell using decontX[71] and scDblFinder.[79] We performed a label transfer from the BICCN/Seattle AD Brain Cell Atlas reference medial temporal gyrus dataset[34] (https://sea-ad-single-cell-profiling.s3.amazonaws.com/MTG/RNAseq/Reference_MTG_RNAseq_final-nuclei.2022-06-07.h5ad) using default settings as recommended in Seurat. We also calculated the proportion of exonic reads/total reads for each cell using the molecule.h5 file provided by CellRanger.

Quality control, integration, clustering, and annotation of snRNA-seq data: To determine the filtering metrics for low quality cells without discarding neuronal cell types disproportionally, we concatenated the cell count matrix (known as filtered matrix provided by CellRanger) across all regions using SCANPY.[78] We identified top 4,000 variable genes with scanpy.pp.highly_variable_genes(flavor = ‘‘Seurat_v3’’, batch_key = ‘‘donor’’). On this subset of variable genes, we trained a scVI[37] model (n_layers = 4, n_hidden = 256, dropout_rate = 0.2, n_latent = 30, gene_likelihood = ‘‘zinb’’) and obtained the latent

representation, UMAP (Uniform Manifold Approximation and Projection) and clustering (leiden,[73] resolution = 0.80) (Figure S12A). For each cluster, we checked the distribution of doublet density score, contamination score and number of genes per cell and cell type labels (obtained from Seurat label transfer above). The doublet clusters can be identified as those with high doublet density score, high contamination score and mixed cell labels (Figures S12B and S12C). The low-quality cell clusters could be identified as that with high exonic ratio, high percentage of mitochondria reads and low total unique molecular identifiers (UMIs). Based on the distribution of the relevant metrics in these clusters, we retained nuclei that passed the cutoff of: doublet density score <2.5, number of genes detected >700, percentage mitochondria <15%, and decontX[71] contamination score <0.7. With this threshold, at least 90% of cells from the other cell clusters (not doublet or low quality) were retained (Figures S12C–S12F). With these nuclei that passed the threshold, we performed same scVI[37] integration as described in the previous step, followed by UMAP and clustering (leiden,[73] resolution = 0.70) to identify neuronal and non-neuronal cells (Figure S12G). We assigned the cell type by taking a majority vote of the cell labels in each cluster (Figure S12H) and checked the identified cell types with a dendrogram and known cell type markers. We could see clear separation of the non-neuronal cells, from inhibitory and excitatory neurons (Figure S12I).

We only retained nuclei from neuronal clusters and tested a grid of parameters for the scVI[37] integration for the final annotation. We evaluated the clustering by checking the median silhouette score against the number of clusters for all the parameters tested. We used a final scVI[37] integration (3,000 variable genes, n_layers = 3, n_hidden = 256, dropout_rate = 0.2, gene_likelihood = ‘‘zinb’’) together with leiden[73] clustering resolution of 0.3 as it has one of the top silhouette index scores for 19 clusters (similar to BICCN[34] reference). Thereafter, based on the predicted labels, we further sub-clustered two clusters to obtain L6b, L6 CT and *Pax6* clusters (Figure 1B and Table 1).

Neuronal subtype annotation of Siletti et al. Dataset: Siletti et al. h5ad files[36] were downloaded from CZ CELLxGENE[90,91] (https://cellxgene.cziscience.com/collections/283d65eb-dd53-496d-adb7-7570c7caa443) and were subset to neuronal cells from the lateral entorhinal cortex (LEC), medial entorhinal cortex (MEC), ITG, medial frontal gyrus (MFG), inferior frontal gyrus (IFG), V2, and V1C. We performed label transfer using k-nearest neighboring.[92] A reference pyNNDescent[76] index was created based on the latent representation space from the scVI[37] model for our dataset (STAR Methods; snRNA-seq). Using the same model specifications, we trained the dataset and obtained a query latent representation, which we queried the reference index for approximate neighbors and inferred the most likely cell label and its associated uncertainty.[93] After labeling cells from the publication using our annotation for each donor and nuclei cluster, we used the predicted labels to check the tissue of origin for cells identified to be from region specific clusters in our data (Table 1).

Pseudobulk expression from single cell data in the current dataset: We obtained the pseudobulk expression for each neuronal subtype from each sample (donor in a region) from the current dataset by summing up raw counts. To reduce the contribution of ambient

RNA, we applied CellBender[68] to each sample's raw, unfiltered count matrix using default settings and used the corrected counts for pseudobulking. All differential gene expression analyses were performed using ambient RNA-corrected counts.

Pseudobulking, differential gene expression analysis, PCA analysis, and GO term enrichment for regional differences: We obtained the pseudobulk expression by summing all the gene counts from all quality-controlled nuclei from each donor and/or brain region assigned to each cluster. To identify genes that showed a significant difference between regions, we performed all pairwise comparisons between the five regions in our study using DESeq2,[72] with sex, age, and Braak stage as covariates. We used genes with an adjusted p-value <0.05 and absolute Log2(Fold Change) > 0.5 as differentially expressed genes between regions. These genes were used to perform PCA (using prcomp[70,74,75] function in the stats[38] package in R) on each pseudobulk sample and the first principal components (PC1) were extracted to check for alignment with EC to V1 orientation (Figure S2B). To obtain a subset of differentially expressed genes that are also present in non-pathology samples, we performed the same pairwise analysis on the Siletti et al.[36] dataset (Figures S2C and S2D). We checked for common significance and fold change direction before keeping the intersection of these sets of differentially expressed genes for performing a similar principal component analysis. GO term enrichment was performed for the common significant genes using enrichGO function from clusterProfiler[69] with the default settings (Figures S2E and S2F).

Differential gene expression analysis and MDS analysis for Braak-associated gene expression changes: With the pseudobulk expression for each cluster in each individual region, we retained only samples with more than 50 cells and genes that have cpm >1.5. We tested for significant associations between gene expression and Braak stage using DESeq2,[72] with sex as a covariate and Braak stage encoded numerically. We performed a Wald test for the continuous variable Braak stage and controlled for false discovery using Storey's[77] method implemented in the R package qvalue.[77] Genes with a q-value <0.05 were considered significantly associated with the term of interest.

An analysis of RIN and PMI's effect on differential gene expression was completed separately from the differential gene expression analysis. RIN and PMI were set as continuous variables (scaled and centered) to the regression model described above. The model was fit for 6 most abundant neuronal subtypes (L2/3, L4, L5, *VIP*, *PVALB* and *SST*). Testing for genes significantly that were associated (q-value <0.05) with RIN or PMI, we observed that for most regions and neuronal subtypes, the number of differentially expressed genes associated with RIN or PMI were relatively low, compared to the number of differently expressed genes associated with Braak stage, except for the PFC, where there is an effect of PMI on differential gene expression (Table S9).

After obtaining gene-wise, Braak-associated fold changes for each neuron subtype in each region, we performed multi-dimensional scaling (MDS) using the cmdscale function from the R package MASS,[70] using a pre-computed Manhattan distance matrix (Figure 2A). For example, we calculated the t statistic for difference in Braak-associated fold changes for each gene between V1 and ITG, across all neuronal subtypes. To identify the key

pathways underlying the difference in Braak-associated fold changes between regions, gene set enrichment analyses (GSEA) were performed on these calculated t statistic-derived genes using clusterProfiler[69] package in R (Figure 2B).

For differences between neuron subtypes in ITG, we performed a Spearman correlation on the commonly detected genes across all neuron subtypes, followed by hierarchical clustering with Ward's minimum variance clustering (ward.D2) method using hclust function in the stats[38] package in R (Figure 2C). To identify the key pathways underlying the difference in Braak-associated fold changes between neuron subtypes, the same GSEA was performed using calculated t statistics for the difference between excitatory and inhibitory neurons. For the example pathways shown (Figure 2D), the average fold change for each gene is calculated for either inhibitory neurons or excitatory neurons and the distribution is visualized with a boxplot. The *p*-value is obtained by testing the null hypothesis that there is no difference in the mean Log2(Fold Change) between excitatory and inhibitory neurons across all genes in the pathway.

Analysis of neuronal subtype abundance: We used scCODA[39] (from the package pertpy[78] in Python) to test for neuron subtype abundance changes across Braak stages and in relationship to pT231/Total Tau ELISA values, pT231 immunoreactivity (percent area of cortical AT180 immunoreactivity), and amyloid-β immunoreactivity (percent area of cortical 3D6 immunoreactivity; ITG data only) levels (Figures 3A, S4B, S4D, and S10C). A subset of anndata[66] was created for every region in our dataset and we performed the scCODA analysis[39] according to the standard procedure (https://pertpy.readthedocs.io/en/latest/tutorials/notebooks/sccoda.html), using sex, age (with 3 categorical bins), and RIN values (3 categorical bins) as covariates. We used the summary[78] function to select neuron subtypes with credible effects (FDR <0.05). All data are presented with 95% confidence intervals.

Differential gene expression analysis for pTau-associated genes: With the pseudobulk expression for each cluster in each individual region, we only retained samples with more than 50 cells and genes that had cpm >1.5. We tested for significant associations between gene expression and pT231/Total Tau ELISA levels (continuous variable range 0–1.0) using DESeq2,[72] with sex as a covariate as we expected sex-related gene expression differences. We performed a Wald test for pT231/Total Tau levels and controlled for false discovery with Storey's[77] method, both implemented in the R package qvalue.[77] Genes with a q-value <0.05 were considered significantly associated with the pT231/Total Tau ELISA levels (Table S4). An MA plot showing significant positive and negative pT231/Total Tau coefficients as identified in L2/3 IT neurons in ITG was made using the DESeq2[72] package in R (Figure 4A). To identify the key pathways underlying difference in pTau-associated genes, GO term enrichment analyses were performed separately on significantly up-regulated genes (FDR <0.05 and Log2(Fold Change) > 0) or down-regulated genes (FDR <0.05 and Log2(Fold Change) < 0) using the clusterProfiler[69] package in R (Figure 4B). The fold changes of upregulated pTau-associated genes were separately analyzed with only cell death-related GO and Reactome[48] terms (all included terms in the analysis listed in Figure

S9) using the same method, with results plotted in a heatmap using Prism 9 (GraphPad) (Figure S9).

Average effects of amyloid-β on GO terms associated with L2/3 IT ITG neuron gene expression: We first tested for significant associations in L2/3 IT ITG neurons between gene expression and amyloid-β immunoreactivity (continuous variable range 0–1.0) using DESeq2,[72] with sex as a covariate. We performed a Wald test for amyloid-β immunoreactivity and controlled for false discovery with Storey's[77] method, both implemented in the R package qvalue.[77] Genes with a q-value <0.05 were considered significantly associated with amyloid-β immunoreactivity levels.

To ensure fold changes from the pTau and amyloid-β regressions were comparable, we scaled both pTau-associated and amyloid-β immunoreactivity-associated values from L2/3 IT ITG neurons with a min-max normalization and regressed the gene expression against these normalized values using DESeq2[72] with the same expression threshold filter with sex as a covariate as described in previous sections. We retrieved the genes falling into the top 3 GO terms associated with all detected in L2/3 IT ITG neurons and compared their distributions stratified by pTau and amyloid-β using a dot and whisker plot (95% confidence interval; Figure S10A).We retrieved the genes falling into the top 3 GO terms associated with pTau in L2/3 IT ITG neurons and compared their distributions stratified by pTau and amyloid-β using a dot and whisker plot (95% confidence interval; Figure S10B).

Analysis of the Otero-Garcia et al. Dataset: Fastq files derived from Otero-Garcia et al.[12] were downloaded (GEO:GSE129308) and processed using the same version of CellRanger used in this study (CellRanger v7.0.1, 10X Genomics). For each individual sample output, we performed the same a label transfer from the BICCN/Seattle AD Brain Cell Atlas reference medial temporal gyrus dataset[34] and preprocessing as described in a previous section (STAR Methods, Processing of snRNA-seq reads and label transfer). We performed one round of scVI[37] integration and identified clusters with majority vote from transferred labels (Figure S13A). We retained cells with doublet density score <3.0 (Figure S13B), a percentage of mitochondrial contamination <15 (Figure S13C) and number of genes detected >700 (Figure S13D). We then removed non-neuronal cells, doublets, and low-quality cells. We performed label transfer from our dataset to the remaining neuronal cells with k-nearest neighboring,[92] as completed for the Siletti et al.[36] analysis (STAR Methods, Neuronal subtype annotation of Siletti et al.[36] dataset). After labeling cells with our annotation (Figure S13E and Table S6), we modeled the proportion of each neuronal subtype using a quasibinomial generalized linear model with the fractions ($AT8^+$ or $AT8^-$) and donor as independent variables. We tested the fraction coefficient with a t test using the summary[78] function and performed FDR adjustment for all *p*-values obtained from this test across all neuronal subtypes. The coefficients and 95% confidence interval (calculated using confint function in the stats[38] package in R) were visualized with a dot and bar plot (Figure 4C and Table S6). The individual donor log odds estimates of the $AT8^+$ vs. AT8-enrichment are visualized as individual data points (dots) (Figures 4D and S7D) and were calculated as: Log(proportion of each neuron subtype in $AT8^+$ fraction/proportion of each neuron subtype

in AT8$^+$ fraction) - Log(proportion of each neuron subtype in AT8-fraction/proportion of each neuron subtype in AT8-fraction).

Analysis of differential gene expression results from Mathys et al. 2023: The differential gene expression results conducted by Mathys et al. 2023[7] on their dataset were downloaded from https://github.com/mathyslab7/ROSMAP_snRNAseq_PFC/tree/main/Results/Differential_gene_expression_analysis. We extracted results associated with different pathology measures: global pathology (gpath), neurofibrillary tangles (nft), amyloid, and plaques. We conducted a Spearman correlation on the genes overlapping between our pTau-associated DEGs in ITG L2/3 neurons and 5 neuronal subtypes from Mathys et al.[7] which were associated with the different pathology measures. Spearman's rank correlation coefficients from the correlations were depicted as a heatmap (Figure S8).

Analysis of Balusu et al. data: The gene expression result tables from xenografted neurons conducted by Balusu et al.[58] were downloaded from Supplementary Material at DOI: https://doi.org/10.1126/science.abp9556. We conducted a Spearman correlation between the Log2(Fold Change) of the genes from the xenografted neurons to the Log2(Fold Change) of genes associated with pTau in L2/3 IT ITG neurons (Figure S11). We then ran a Fisher's exact test, comparing the positive and negative pT231-associated gene fold changes from our ITG L2/3 IT neurons to positive and negative gene fold changes of the xenografted neurons, respectively (Table S7).

Integration of snRNA-seq data from current study and spatial data from Chen et al: The expected abundance of cell subtypes across spatial spots was calculated using cell2location (v0.1.3).[67] Reference expression signatures of cell subtypes were estimated using our snRNA-seq dataset from the ITG region, employing scVI[37]-tools (v1.0.4) wrapped in the cell2location.models. RegressionModel function with the sample name as the batch key. The Visium (10X Genomics) spatial dataset from Chen et al.,[40] including gene expression counts and histological images from 3 AD samples and 3 control samples, was downloaded from the GEO database (GEO: GSE220442). Before estimation, genes detected in fewer than 5 cells were excluded. The wrapped model was trained with a maximum of 250 epochs, and a final reference matrix was generated by averaging the estimations. Subsequently, spatial transcriptomic data from each slide from Chen et al.[40] was deconvoluted using hierarchical Bayesian models, as wrapped in the Cell2location[67] function. We utilized the following parameters for training: N_cells_per_location = 5, detection_alpha = 20, max_epochs = 30000, batch_size = None, and train_size = 1. Expected cell subtype abundance across all spots was then generated. The sc.pl.spatial function from SCANPY[78] (v1.9.8) was used to visualize the cell annotation and single gene expression across spatial coordinates. To compare the cortical layer specificity of subtypes, we calculated the mean abundance for each subtype and layer annotated by Chen et al.[40] (Figures 3G and S6).

Creation of apoptosis pathway map of pTau-associated L2/3 IT ITG DEGs: The apoptosis pathway diagram, colored by pTau-associated Log2(Fold Change) from ITG

L2/3 IT neurons, was generated with the SBGNview[44,45] package in R and the apoptosis signaling pathway (PANTHER: P00006) from the PANTHER[46] database (Figure 4E).

Fluorescent multiplexed FISH/IHC, AT180 IHC, and 3D6 IHC image analysis: Of the 30 donor samples used for fluorescent multiplexed FISH/IHC, 4 samples were eliminated from quantification due to poor tissue quality (Table S1). Image analysis for fluorescent FISH/IHC images was conducted using modules in HALO (FISH v2.2.0, ISH v3.4.8; Indica Labs) with customized quantification settings. Object data output from HALO analyses was further analyzed with R using custom scripts and visualized using the ggplot2 package[94] and Prism 9 (GraphPad). For FISH/IHC statistical analysis, a simple linear regression was run between numbers of NeuN+, *CBLN2*+, and *LINC00507*+ nuclei (L2/3 IT ITG-aligning neurons) and AT180 integrated intensity (Figure 3D). Additionally, a Shapiro-Wilk test was used to test dataset normality and two-way Wilcoxon matchedpairs signed rank tests were used (Figures 3E and 3F). L2/3 IT neuron identity was determined in R as having any number of *LINC00507* copies and higher than the mean *CBLN2* copy numbers as determined by averaging all copy numbers for each nucleus across all donor tissue sections. Images were formatted for publication using Adobe Illustrator CC (Adobe).

For AT180 IHC quantification of cortical image area, percent area of cortical tissue occupied by AT180 immunoreactivity was measured using a module in HALO (Area Quantification v2.4.2; Indica Labs) with customized quantification settings. Three donor sections from the 30 donors were eliminated from quantification due to poor tissue quality ($N = 27$; Table S1). The same procedure conducted for AT180 IHC was conducted for 3D6 IHC. A total of 116 slides were produced from all available brain regions from the 30 donors for 3D6 IHC. Nine slides (EC:4, ITG:1, PFC:2, V1:2) were eliminated from quantification due to poor tissue quality (Table S1). Percent area of AT180 and 3D6 immunopositivity (ITG only) were used for scCODA[39] analysis (Figures S4D and S10C; STAR Methods; Analysis of neuronal subtype abundance). Percent area of AT180 immunoreactivity were correlated to pT231/Total Tau ELISA values with a two-tailed Spearman correlation (Figure S4E).

Statistics, figure making, and statistical software: Unless otherwise specified, Spearman rank correlation tests were used for correlations and tested for significance using a two-tailed test with *p*-values approximated using a Student's t-distribution. All plots made in R, unless otherwise specified, were created using the ggplot2 package.[94] Images, graphs, and figures were created with R, Prism 9 (GraphPad), Adobe Illustrator CC (Adobe), and/or in BioRender (https://BioRender.com/5id4dwz). Statistics were run in R or Prism 9 (GraphPad).

Supplementary Material

Refer to Web version on PubMed Central for supplementary material.

ACKNOWLEDGMENTS

We would like to acknowledge individuals who have assisted in completing this project, including Patrick Dooley and Teresa Connors for their help with tissue selection, Derek Oakley for neuropathological expertise, Simon Dujardin for wet lab work, and Emily J. McGlame for completing IHC. We also thank the many research

participants and their families who participated in research conducted at the Massachusetts Alzheimer's Disease Research Center. This work was supported by NIH grants R01AG071567 (R.E.B.), P30AG062421 (B.T.H., M.P.F., A.S.-P., and S.D.), K08AG064039 (A.S.-P.), and MassCATS.

REFERENCES

1. Gómez-Isla T, Hollister R, West H, Mui S, Growdon JH, Petersen RC, Parisi JE, and Hyman BT (1997). Neuronal loss correlates with but exceeds neurofibrillary tangles in Alzheimer's disease. Ann. Neurol 41, 17–24. 10.1002/ana.410410106. [PubMed: 9005861]
2. Schäfer A, Chaggar P, Thompson TB, Goriely A, Kuhl E, and Initiative, the A.D.N. (2021). Predicting brain atrophy from tau pathology: a summary of clinical findings and their translation into personalized models. Brain Multiphysics 2, 100039. 10.1016/j.brain.2021.100039.
3. Braak H, and Braak E (1991). Neuropathological stageing of Alzheimer-related changes. Acta Neuropathol 82, 239–259. 10.1007/bf00308809. [PubMed: 1759558]
4. Ossenkoppele R, Schonhaut DR, Schöll M, Lockhart SN, Ayakta N, Baker SL, O'Neil JP, Janabi M, Lazaris A, Cantwell A, et al. (2016). Tau PET patterns mirror clinical and neuroanatomical variability in Alzheimer's disease. Brain 139, 1551–1567. 10.1093/brain/aww027. [PubMed: 26962052]
5. Thompson PM, Hayashi KM, de Zubicaray G, Janke AL, Rose SE, Semple J, Herman D, Hong MS, Dittmer SS, Doddrell DM, and Toga AW (2003). Dynamics of Gray Matter Loss in Alzheimer's Disease. J. Neurosci 23, 994–1005. 10.1523/jneurosci.23-03-00994.2003. [PubMed: 12574429]
6. Dickerson BC, Bakkour A, Salat DH, Feczko E, Pacheco J, Greve DN, Grodstein F, Wright CI, Blacker D, Rosas HD, et al. (2009). The Cortical Signature of Alzheimer's Disease: Regionally Specific Cortical Thinning Relates to Symptom Severity in Very Mild to Mild AD Dementia and is Detectable in Asymptomatic Amyloid-Positive Individuals. Cereb. Cortex 19, 497–510. 10.1093/cercor/bhn113. [PubMed: 18632739]
7. Mathys H, Peng Z, Boix CA, Victor MB, Leary N, Babu S, Abdelhady G, Jiang X, Ng AP, Ghafari K, et al. (2023). Single-cell atlas reveals correlates of high cognitive function, dementia, and resilience to Alzheimer's disease pathology. Cell 186, 4365–4385. 10.1016/j.cell.2023.08.039. [PubMed: 37774677]
8. Mathys H, Davila-Velderrain J, Peng Z, Gao F, Mohammadi S, Young JZ, Menon M, He L, Abdurrob F, Jiang X, et al. (2019). Single-cell transcriptomic analysis of Alzheimer's disease. Nature 570, 332–337. 10.1038/s41586-019-1195-2. [PubMed: 31042697]
9. Gazestani V, Kamath T, Nadaf NM, Dougalis A, Burris SJ, Rooney B, Junkkari A, Vanderburg C, Pelkonen A, Gomez-Budia M, et al. (2023). Early Alzheimer's disease pathology in human cortex involves transient cell states. Cell 186, 4438–4453. 10.1016/j.cell.2023.08.005. [PubMed: 37774681]
10. Gabitto MI, Travaglini KJ, Rachleff VM, Kaplan ES, Long B, Ariza J, Ding Y, Mahoney JT, Dee N, Goldy J, et al. (2024). Integrated multimodal cell atlas of Alzheimer's disease. Nat. Neurosci 27, 2366–2383. 10.1038/s41593-024-01774-5. [PubMed: 39402379]
11. Wachter A, Woodbury ME, Lombardo S, Abdourahman A, Wuest C, McGlame E, Pastika T, Tamm J, Romanul N, Yanamandra K, et al. (2024). Landscape of brain myeloid cell transcriptome along the spatiotemporal progression of Alzheimer's disease reveals distinct sequential responses to Aβ and tau. Acta Neuropathol 147, 65. 10.1007/s00401-024-02704-2. [PubMed: 38557897]
12. Otero-Garcia M, Mahajani SU, Wakhloo D, Tang W, Xue Y-Q, Morabito S, Pan J, Oberhauser J, Madira AE, Shakouri T, et al. (2022). Molecular signatures underlying neurofibrillary tangle susceptibility in Alzheimer's disease. Neuron 110, 2929–2948. 10.1016/j.neuron.2022.06.021. [PubMed: 35882228]
13. Sadick JS, O'Dea MR, Hasel P, Dykstra T, Faustin A, and Liddelow SA (2022). Astrocytes and oligodendrocytes undergo subtype-specific transcriptional changes in Alzheimer's disease. Neuron 110, 1788–1805. 10.1016/j.neuron.2022.03.008. [PubMed: 35381189]
14. Lau S-F, Cao H, Fu AKY, and Ip NY (2020). Single-nucleus transcriptome analysis reveals dysregulation of angiogenic endothelial cells and neuroprotective glia in Alzheimer's disease. Proc. Natl. Acad. Sci 117, 25800–25809. 10.1073/pnas.2008762117. [PubMed: 32989152]

15. Gerrits E, Brouwer N, Kooistra SM, Woodbury ME, Vermeiren Y, Lambourne M, Mulder J, Kummer M, Möller T, Biber K, et al. (2021). Distinct amyloid-β and tau-associated microglia profiles in Alzheimer's disease. Acta Neuropathol 141, 681–696. 10.1007/s00401-021-02263-w. [PubMed: 33609158]

16. Smith AM, Davey K, Tsartsalis S, Khozoie C, Fancy N, Tang SS, Liaptsi E, Weinert M, McGarry A, Muirhead RCJ, et al. (2022). Diverse human astrocyte and microglial transcriptional responses to Alzheimer's pathology. Acta Neuropathol 143, 75–91. 10.1007/s00401-021-02372-6. [PubMed: 34767070]

17. Leng K, Li E, Eser R, Piergies A, Sit R, Tan M, Neff N, Li SH, Rodriguez RD, Suemoto CK, et al. (2021). Molecular characterization of selectively vulnerable neurons in Alzheimer's disease. Nat. Neurosci 24, 276–287. 10.1038/s41593-020-00764-7. [PubMed: 33432193]

18. Alsema AM, Jiang Q, Kracht L, Gerrits E, Dubbelaar ML, Miedema A, Brouwer N, Hol EM, Middeldorp J, van Dijk R, et al. (2020). Profiling microglia from Alzheimer's disease donors and non-demented elderly in acute human postmortem cortical tissue. Front. Mol. Neurosci 13, 134. 10.3389/fnmol.2020.00134. [PubMed: 33192286]

19. Grubman A, Chew G, Ouyang JF, Sun G, Choo XY, McLean C, Simmons RK, Buckberry S, Vargas-Landin DB, Poppe D, et al. (2019). A single-cell atlas of entorhinal cortex from individuals with Alzheimer's disease reveals cell-type-specific gene expression regulation. Nat. Neurosci 22, 2087–2097. 10.1038/s41593-019-0539-4. [PubMed: 31768052]

20. Bennett DA, Buchman AS, Boyle PA, Barnes LL, Wilson RS, and Schneider JA (2018). Religious Orders Study and Rush Memory and Aging Project. J Alzheimer's Dis 64, S161–S189. 10.3233/jad-179939. [PubMed: 29865057]

21. Yang AC, Vest RT, Kern F, Lee DP, Agam M, Maat CA, Losada PM, Chen MB, Schaum N, Khoury N, et al. (2022). A human brain vascular atlas reveals diverse mediators of Alzheimer's risk. Nature 603, 885–892. 10.1038/s41586-021-04369-3. [PubMed: 35165441]

22. Thrupp N, Frigerio CS, Wolfs L, Skene NG, Fattorelli N, Poovathingal S, Fourne Y, Matthews PM, Theys T, Mancuso R, et al. (2020). Single-Nucleus RNA-Seq Is Not Suitable for Detection of Microglial Activation Genes in Humans. Cell Rep 32, ■■. 10.1016/j.celrep.2020.108189.

23. Del-Aguila JL, Li Z, Dube U, Mihindukulasuriya KA, Budde JP, Fernandez MV, Ibanez L, Bradley J, Wang F, Bergmann K, et al. (2019). A single-nuclei RNA sequencing study of Mendelian and sporadic AD in the human brain. Alzheimers Res. Ther 11, 71. 10.1186/s13195-019-0524-x. [PubMed: 31399126]

24. Morabito S, Miyoshi E, Michael N, Shahin S, Martini AC, Head E, Silva J, Leavy K, Perez-Rosendahl M, and Swarup V (2021). Single-nucleus chromatin accessibility and transcriptomic characterization of Alzheimer's disease. Nat. Genet 53, 1143–1155. 10.1038/s41588-021-00894-z. [PubMed: 34239132]

25. Zhou Y, Song WM, Andhey PS, Swain A, Levy T, Miller KR, Poliani PL, Cominelli M, Grover S, Gilfillan S, et al. (2020). Human and mouse single-nucleus transcriptomics reveal TREM2-dependent and TREM2-independent cellular responses in Alzheimer's disease. Nat. Med 26, 131–142. 10.1038/s41591-019-0695-9. [PubMed: 31932797]

26. Zhou Y, Su Y, Li S, Kennedy BC, Zhang DY, Bond AM, Sun Y, Jacob F, Lu L, Hu P, et al. (2022). Molecular landscapes of human hippocampal immature neurons across lifespan. Nature 607, 527–533. 10.1038/s41586-022-04912-w. [PubMed: 35794479]

27. Braak H, and Braak E (1991). Demonstration of Amyloid Deposits and Neurofibrillary Changes in Whole Brain Sections. Brain Pathol 1, 213–216. 10.1111/j.1750-3639.1991.tb00661.x. [PubMed: 1669710]

28. Braak H, Alafuzoff I, Arzberger T, Kretzschmar H, and Del Tredici K (2006). Staging of Alzheimer disease-associated neurofibrillary pathology using paraffin sections and immunocytochemistry. Acta Neuropathol 112, 389–404. 10.1007/s00401-006-0127-z. [PubMed: 16906426]

29. Braak H, and Tredici KD (2018). Spreading of Tau Pathology in Sporadic Alzheimer's Disease Along Cortico-cortical Top-Down Connections. Cereb Cortex New York Ny 28, 3372–3384. 10.1093/cer-cor/bhy152.

30. Arnold SE, Hyman BT, Flory J, Damasio AR, and Van Hoesen GW (1991). The Topographical and Neuroanatomical Distribution of Neurofibrillary Tangles and Neuritic Plaques in the Cerebral

Cortex of Patients with Alzheimer's Disease. Cereb. Cortex 1, 103–116. 10.1093/cercor/1.1.103. [PubMed: 1822725]

31. Braak H, and Braak E (1994). Morphological criteria for the recognition of Alzheimer's disease and the distribution pattern of cortical changes related to this disorder. Neurobiol. Aging 15, 355–380. 10.1016/0197-4580(94)90032-9. [PubMed: 7936061]
32. Serrano-Pozo A, Frosch MP, Masliah E, and Hyman BT (2011). Neuropathological alterations in Alzheimer disease. Cold Spring Harb. Perspect. Med 1, a006189. [PubMed: 22229116]
33. Montine TJ, Phelps CH, Beach TG, Bigio EH, Cairns NJ, Dick-son DW, Duyckaerts C, Frosch MP, Masliah E, Mirra SS, et al. (2012). National Institute on Aging-Alzheimer's Association guidelines for the neuropathologic assessment of Alzheimer's disease: a practical approach. Acta Neuropathol 123, 1–11. 10.1007/s00401-011-0910-3. [PubMed: 22101365]
34. Jorstad NL, Close J, Johansen N, Yanny AM, Barkan ER, Travaglini KJ, Bertagnolli D, Campos J, Casper T, Crichton K, et al. (2023). Transcriptomic cytoarchitecture reveals principles of human neocortex organization. Science 382, eadf6812. 10.1126/science.adf6812. [PubMed: 37824655]
35. Borm LE, Mossi Albiach A, Mannens CCA, Janusauskas J, Özgün C, Fernández-García D, Hodge R, Castillo F, Hedin CRH, Villa-blanca EJ, et al. (2023). Scalable in situ single-cell profiling by electrophoretic capture of mRNA using EEL FISH. Nat. Biotechnol 41, 222–231. 10.1038/s41587-022-01455-3. [PubMed: 36138169]
36. Siletti K, Hodge R, Mossi Albiach A, Lee KW, Ding S-L, Hu L, Lönnerberg P, Bakken T, Casper T, Clark M, et al. (2023). Transcriptomic diversity of cell types across the adult human brain. Science 382, eadd7046. 10.1126/science.add7046. [PubMed: 37824663]
37. Lopez R, Regier J, Cole MB, Jordan MI, and Yosef N (2018). Deep generative modeling for single-cell transcriptomics. Nat. Methods 15, 1053–1058. 10.1038/s41592-018-0229-2. [PubMed: 30504886]
38. Team RC (2023). R: A Language and Environment for Statistical Computing (R Foundation for Statistical Computing).
39. Büttner M, Ostner J, Müller CL, Theis FJ, and Schubert B (2021). scCODA is a Bayesian model for compositional single-cell data analysis. Nat. Commun 12, 6876. 10.1038/s41467-021-27150-6. [PubMed: 34824236]
40. Chen S, Chang Y, Li L, Acosta D, Li Y, Guo Q, Wang C, Turkes E, Morrison C, Julian D, et al. (2022). Spatially resolved transcriptomics reveals genes associated with the vulnerability of middle temporal gyrus in Alzheimer's disease. Acta Neuropathol. Commun 10, 188. 10.1186/s40478-022-01494-6. [PubMed: 36544231]
41. Gómez-Isla T, Price JL Jr., Hyman BTDWM, McKeel DW Jr., Morris JC, and Growdon JH (1996). Profound Loss of Layer II Entorhinal Cortex Neurons Occurs in Very Mild Alzheimer's Disease. J. Neurosci 16, 4491–4500. 10.1523/jneurosci.16-14-04491.1996. [PubMed: 8699259]
42. Hodge RD, Bakken TE, Miller JA, Smith KA, Barkan ER, Gray-buck LT, Close JL, Long B, Johansen N, Penn O, et al. (2019). Conserved cell types with divergent features in human vs. mouse cortex. Nature 573, 61–68. 10.1038/s41586-019-1506-7. [PubMed: 31435019]
43. Luria V, Ma S, Shibata M, Pattabiraman K, and Sestan N (2023). Molecular and cellular mechanisms of human cortical connectivity. Curr. Opin. Neurobiol 80, 102699. 10.1016/j.conb.2023.102699. [PubMed: 36921362]
44. Dong X, Vegesna K, Brouwer C, and Luo W (2022). SBGNview: towards data analysis, integration and visualization on all pathways. Bioinformatics 38, 1473–1476. 10.1093/bioinformatics/btab793. [PubMed: 34864890]
45. Luo W, and Brouwer C (2013). Pathview: an R/Bioconductor package for pathway-based data integration and visualization. Bioinformatics 29, 1830–1831. 10.1093/bioinformatics/btt285. [PubMed: 23740750]
46. Thomas PD, Ebert D, Muruganujan A, Mushayahama T, Albou LP, and Mi H (2022). PANTHER: Making genome-scale phylogenetics accessible to all. Protein Sci 31, 8–22. 10.1002/pro.4218. [PubMed: 34717010]
47. Hildyard JCW, Rawson F, Wells DJ, and Piercy RJ (2020). Multiplex in situ hybridization within a single transcript: RNAscope reveals dystrophin mRNA dynamics. PLoS One 15, e0239467. 10.1371/journal.pone.0239467. [PubMed: 32970731]

48. Wu G, and Haw R (2017). Functional interaction network construction and analysis for disease discovery. Methods Mol. Biol 1558, 235–253. 10.1007/978-1-4939-6783-4_11. [PubMed: 28150241]

49. Chen S, Acosta D, Li L, Liang J, Chang Y, Wang C, Fitzgerald J, Morrison C, Goulbourne CN, Nakano Y, et al. (2022). Wolframin is a novel regulator of tau pathology and neurodegeneration. Acta Neuropathol 143, 547–569. 10.1007/s00401-022-02417-4. [PubMed: 35389045]

50. Delpech J-C, Pathak D, Varghese M, Kalavai SV, Hays EC, Hof PR, Johnson WE, Ikezu S, Medalla M, Luebke JI, and Ikezu T (2021). Wolframin-1–expressing neurons in the entorhinal cortex propagate tau to CA1 neurons and impair hippocampal memory in mice. Sci. Transl. Med 13, eabe8455. 10.1126/scitranslmed.abe8455. [PubMed: 34524859]

51. Rodriguez-Rodriguez P, Arroyo-Garcia LE, Tsagkogianni C, Li L, Wang W, Végvári Á, Salas-Allende I, Plautz Z, Cedazo-Minguez A, Sinha SC, et al. (2024). A cell autonomous regulator of neuronal excitability modulates tau in Alzheimer's disease vulnerable neurons. Brain 147, 2384–2399. 10.1093/brain/awae051. [PubMed: 38462574]

52. Farrell K, Kim S, Han N, Iida MA, Gonzalez EM, Otero-Garcia M, Walker JM, Richardson TE, Renton AE, Andrews SJ, et al. (2022). Genome-wide association study and functional validation implicates JADE1 in tauopathy. Acta Neuropathol 143, 33–53. 10.1007/s00401-021-02379-z. [PubMed: 34719765]

53. Fu H, Possenti A, Freer R, Nakano Y, Hernandez Villegas NC, Tang M, Cauhy PVM, Lassus BA, Chen S, Fowler SL, et al. (2019). A tau homeostasis signature is linked with the cellular and regional vulnerability of excitatory neurons to tau pathology. Nat. Neurosci 22, 47–56. 10.1038/s41593-018-0298-7. [PubMed: 30559469]

54. Mathys H, Boix CA, Akay LA, Xia Z, Davila-Velderrain J, Ng AP, Jiang X, Abdelhady G, Galani K, Mantero J, et al. (2024). Single-cell multiregion dissection of Alzheimer's disease. Nature 632, 858–868. 10.1038/s41586-024-07606-7. [PubMed: 39048816]

55. Chen XQ, Sawa M, Becker A, Karachentsev D, Zuo X, Rynearson KD, Tanzi RE, and Mobley WC (2023). Retromer Proteins Reduced in Down Syndrome and the Dp16 Model: Impact of APP Dose and Preclinical Studies of a γ-Secretase Modulator. Ann. Neurol 94, 245–258. 10.1002/ana.26659. [PubMed: 37042072]

56. Qureshi YH, Berman DE, Marsh SE, Klein RL, Patel VM, Simoes S, Kannan S, Petsko GA, Stevens B, and Small SA (2022). The neuronal retromer can regulate both neuronal and microglial phenotypes of Alzheimer's disease. Cell Rep 38, 110262. 10.1016/j.celrep.2021.110262. [PubMed: 35045281]

57. Simoes S, Guo J, Buitrago L, Qureshi YH, Feng X, Kothiya M, Cortes E, Patel V, Kannan S, Kim Y-H, et al. (2021). Alzheimer's vulnerable brain region relies on a distinct retromer core dedicated to endosomal recycling. Cell Rep 37, 110182. 10.1016/j.celrep.2021.110182. [PubMed: 34965419]

58. Balusu S, Horré K, Thrupp N, Craessaerts K, Snellinx A, Serneels L, T'Syen D, Chrysidou I, Arranz AM, Sierksma A, et al. (2023). MEG3 activates necroptosis in human neuron xenografts modeling Alzheimer's disease. Science 381, 1176–1182. 10.1126/science.abp9556. [PubMed: 37708272]

59. Hyman BT, Van Hoesen GW, Damasio AR, and Barnes CL (1984). Alzheimer's Disease: Cell-Specific Pathology Isolates the Hippocampal Formation. Science 225, 1168–1170. 10.1126/science.6474172. [PubMed: 6474172]

60. Balusu S, Praschberger R, Lauwers E, De Strooper B, and Verstreken P (2023). Neurodegeneration cell per cell. Neuron 111, 767–786. 10.1016/j.neuron.2023.01.016. [PubMed: 36787752]

61. Zhao X, Kotilinek LA, Smith B, Hlynialuk C, Zahs K, Ramsden M, Cleary J, and Ashe KH (2016). Caspase-2 cleavage of tau reversibly impairs memory. Nat. Med 22, 1268–1276. 10.1038/nm.4199. [PubMed: 27723722]

62. Bryant A, Li Z, Jayakumar R, Serrano-Pozo A, Woost B, Hu M, Woodbury ME, Wachter A, Lin G, Kwon T, et al. (2023). Endothelial Cells Are Heterogeneous in Different Brain Regions and Are Dramatically Altered in Alzheimer's Disease. J. Neurosci 43, 4541–4557. 10.1523/jneurosci.0237-23.2023. [PubMed: 37208174]

63. Serrano-Pozo A, Li Z, Woodbury ME, Muñoz-Castro C, Wachter A, Jayakumar R, Bryant AG, Noori A, Welikovitch LA, Hu M, et al. (2023). Astrocyte transcriptomic changes along the

spatiotemporal progression of Alzheimer's disease. Alzheimer's Dement 19, e075148. 10.1002/alz.075148.

64. Telpoukhovskaia MA, Hadad N, Gurdon B, Dai Y, Ouellette AR, Neuner SM, Dunn AR, Willcox JAL, Wu Y, Dumitrescu L, et al. (2023). Conserved cell-type specific signature of resilience to Alzheimer's disease nominates role for excitatory intratelencephalic cortical neurons. Preprint at bioRxiv. 10.1101/2022.04.12.487877.
65. Green GS, Fujita M, Yang H-S, Taga M, McCabe C, Cain A, White CC, Schmidtner AK, Zeng L, Wang Y, et al. (2023). Cellular dynamics across aged human brains uncover a multicellular cascade leading to Alz-heimer's disease. Preprint at bioRxiv. 10.1101/2023.03.07.531493.
66. Virshup I, Rybakov S, Theis FJ, Angerer P, and Wolf FA (2021). anndata: Annotated data. Preprint at bioRxiv. 10.1101/2021.12.16.473007.
67. Kleshchevnikov V, Shmatko A, Dann E, Aivazidis A, King HW, Li T, Elmentaite R, Lomakin A, Kedlian V, Gayoso A, et al. (2022). Cell2location maps fine-grained cell types in spatial transcriptomics. Nat. Biotechnol 40, 661–671. 10.1038/s41587-021-01139-4. [PubMed: 35027729]
68. Fleming SJ, Chaffin MD, Arduini A, Akkad A-D, Banks E, Marioni JC, Philippakis AA, Ellinor PT, and Babadi M (2023). Unsupervised removal of systematic background noise from droplet-based single-cell experiments using CellBender. Nat. Methods 20, 1323–1335. 10.1038/s41592-023-01943-7. [PubMed: 37550580]
69. Yu G, Wang L-G, Han Y, and He Q-Y (2012). clusterProfiler: an R Package for Comparing Biological Themes Among Gene Clusters. Omics J Integr Biology 16, 284–287. 10.1089/omi.2011.0118.
70. Venables WN, and Ripley BD (2002). Modern Applied Statistics with S (Statistics and Computing) (Springer).
71. Yang S, Corbett SE, Koga Y, Wang Z, Johnson WE, Yajima M, and Campbell JD (2020). Decontamination of ambient RNA in single-cell RNA-seq with DecontX. Genome Biol 21, 57. 10.1186/s13059-020-1950-6. [PubMed: 32138770]
72. Love MI, Huber W, and Anders S (2014). Moderated estimation of fold change and dispersion for RNA-seq data with DESeq2. Genome Biol 15, 550. 10.1186/s13059-014-0550-8. [PubMed: 25516281]
73. Traag VA, Waltman L, and Eck N.J. van (2019). From Louvain to Leiden: guaranteeing well-connected communities. Sci Rep-uk 9, 5233. 10.1038/s41598-019-41695-z.
74. Mardia KV, Kent JT, and Bibby JM (1980). Multivariate Analysis (Probability and Mathematical Statistics) (Academic Press).
75. Becker RA, Chambers JM, and Wilks AR (1988). The New S Language: A Programming Environment for Data Analysis and Graphics (Chapman & Hall).
76. Dong W, Moses C, and Li K (2011). Efficient k-nearest neighbor graph construction for generic similarity measures. In WWW'11: Proceedings of 20th International Conference on World wide web, pp. 577–586. 10.1145/1963405.1963487.
77. Storey J, Bass A, Dabney A, and Robinson D (2022). qvalue: R package to estimate q-values and false discovery rate quantities. https://github.com/StoreyLab/qvalue.
78. Wolf FA, Angerer P, and Theis FJ (2018). SCANPY: large-scale single-cell gene expression data analysis. Genome Biol 19, 15. 10.1186/s13059-017-1382-0. [PubMed: 29409532]
79. Germain P-L, Lun A, Garcia Meixide C, Macnair W, and Robinson MD (2021). Doublet identification in single-cell sequencing data using scDblFinder. F1000Res 10, 979. 10.12688/f1000research.73600.2. [PubMed: 35814628]
80. Hafemeister C, and Satija R (2019). Normalization and variance stabilization of single-cell RNA-seq data using regularized negative binomial regression. Genome Biol 20, 296. 10.1186/s13059-019-1874-1. [PubMed: 31870423]
81. Choudhary S, and Satija R (2022). Comparison and evaluation of statistical error models for scRNA-seq. Genome Biol 23, 27. 10.1186/s13059-021-02584-9. [PubMed: 35042561]
82. Hao Y, Stuart T, Kowalski MH, Choudhary S, Hoffman P, Hartman A, Srivastava A, Molla G, Madad S, Fernandez-Granda C, and Satija R (2024). Dictionary learning for

integrative, multimodal and scalable single-cell analysis. Nat. Biotechnol 42, 293–304. 10.1038/s41587-023-01767-y. [PubMed: 37231261]

83. Hao Y, Hao S, Andersen-Nissen E, Mauck WM, Zheng S, Butler A, Lee MJ, Wilk AJ, Darby C, Zager M, et al. (2021). Integrated analysis of multimodal single-cell data. Cell 184, 3573–3587. 10.1016/j.cell.2021.04.048. [PubMed: 34062119]
84. Stuart T, Butler A, Hoffman P, Hafemeister C, Papalexi E, Mauck WM, Hao Y, Stoeckius M, Smibert P, and Satija R (2019). Comprehensive Integration of Single-Cell Data. Cell 177, 1888–1902. 10.1016/j.cell.2019.05.031. [PubMed: 31178118]
85. Butler A, Hoffman P, Smibert P, Papalexi E, and Satija R (2018). Integrating single-cell transcriptomic data across different conditions, technologies, and species. Nat. Biotechnol 36, 411–420. 10.1038/nbt.4096. [PubMed: 29608179]
86. Satija R, Farrell JA, Gennert D, Schier AF, and Regev A (2015). Spatial reconstruction of single-cell gene expression data. Nat. Biotechnol 33, 495–502. 10.1038/nbt.3192. [PubMed: 25867923]
87. Hyman BT, Phelps CH, Beach TG, Bigio EH, Cairns NJ, Carrillo MC, Dickson DW, Duyckaerts C, Frosch MP, Masliah E, et al. (2012). National Institute on Aging-Alzheimer's Association guidelines for the neuropathologic assessment of Alzheimer's disease. Alzheimer's Dement 8, 1–13. 10.1016/j.jalz.2011.10.007. [PubMed: 22265587]
88. Yanamandra K, Kfoury N, Jiang H, Mahan TE, Ma S, Maloney SE, Wozniak DF, Diamond MI, and Holtzman DM (2013). Anti-Tau Antibodies that Block Tau Aggregate Seeding In Vitro Markedly Decrease Pathology and Improve Cognition In Vivo. Neuron 80, 402–414. 10.1016/j.neuron.2013.07.046. [PubMed: 24075978]
89. Holmes BB, Furman JL, Mahan TE, Yamasaki TR, Mirbaha H, Eades WC, Belaygorod L, Cairns NJ, Holtzman DM, and Diamond MI (2014). Proteopathic tau seeding predicts tauopathy in vivo. Proc National Acad Sci 111, E4376–E4385. 10.1073/pnas.1411649111.
90. Abdulla S, Aevermann B, Assis P, Badajoz S, Bell SM, Bezzi E, Cakir B, Chaffer J, Chambers S, Michael Cherry J, et al. (2023). CZ CELL×GENE Discover: A single-cell data platform for scalable exploration, analysis and modeling of aggregated data. Preprint at bioRxiv. 10.1101/2023.10.30.563174.
91. Megill C, Martin B, Weaver C, Bell S, Prins L, Badajoz S, McCandless B, Pisco AO, Kinsella M, Griffin F, et al. (2021). cellxgene: a performant, scalable exploration platform for high dimensional sparse matrices. Preprint at bioRxiv. 10.1101/2021.04.05.438318.
92. Sikkema L, Ramírez-Suástegui C, Strobl DC, Gillett TE, Zappia L, Madissoon E, Markov NS, Zaragosi L-E, Ji Y, Ansari M, et al. (2023). An integrated cell atlas of the lung in health and disease. Nat. Med 29, 1563–1577. 10.1038/s41591-023-02327-2. [PubMed: 37291214]
93. Xu C, Lopez R, Mehlman E, Regier J, Jordan MI, and Yosef N (2021). Probabilistic harmonization and annotation of single-cell transcriptomics data with deep generative models. Mol. Syst. Biol 17, e9620. 10.15252/msb.20209620. [PubMed: 33491336]
94. Wickham H (2011). ggplot2. WIREs Computational Stats. 3, 180–185. 10.1002/wics.147.

Highlights

- snRNA-seq and tau immunoassays in disease-associated regions of AD and non-AD brains
- Identification of tau-vulnerable neuron population in the inferior temporal cortex
- Gene-expression analyses uncover genes linked to apoptosis and cell disassembly

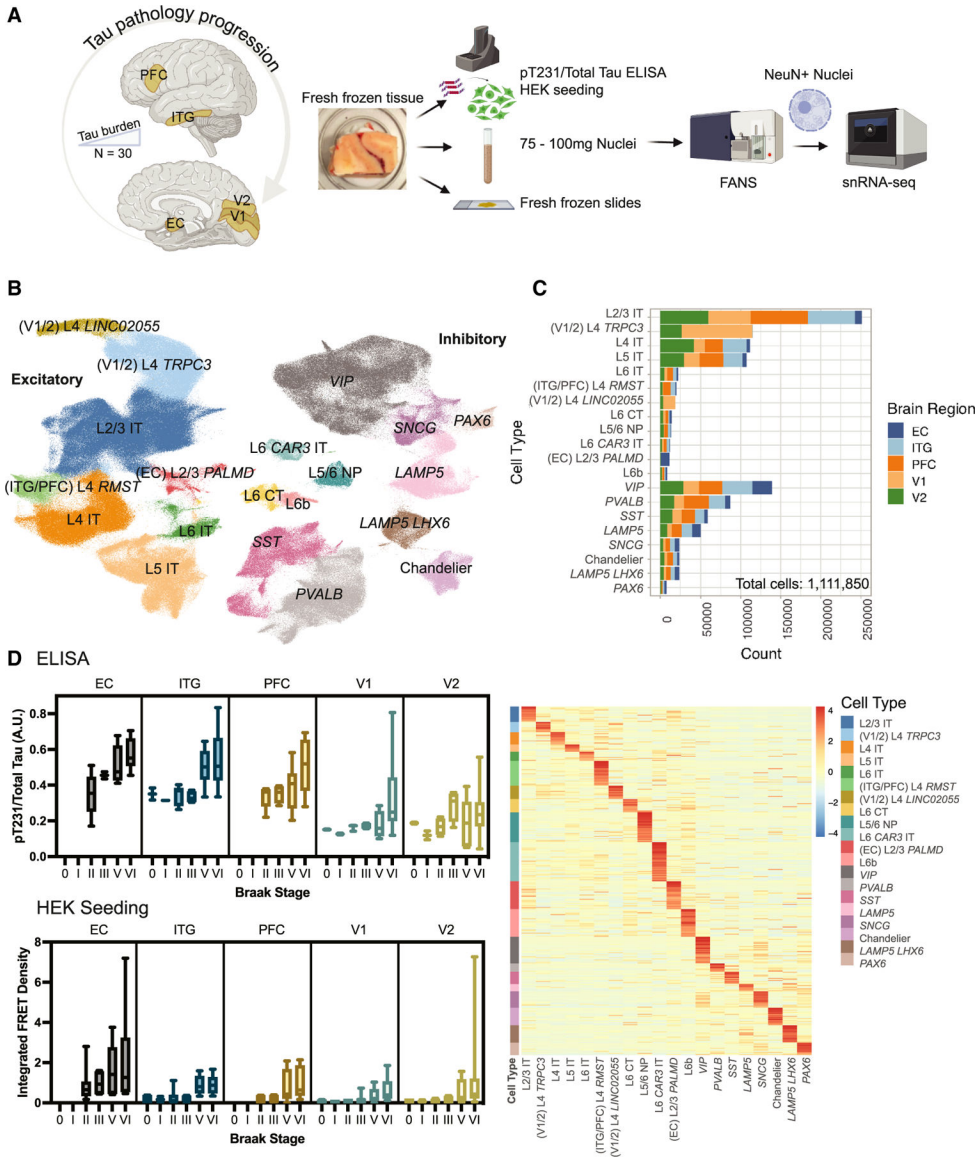

Figure 1. Single-nuclei RNA-seq results from 30 control and AD donors

(A) Cortical samples were taken from five brain regions corresponding to the spread of tau pathology during typical AD progression (EC, entorhinal cortex; ITG, inferior temporal gyrus; PFC, prefrontal cortex; V2, secondary visual cortex; V1, primary visual cortex). Nuclei derived from these samples were sorted for NeuN positivity before snRNA-seq. Cortical tissue samples were analyzed by pT231/Total Tau ELISA and HEK seeding assays. Fresh frozen slides were cut from each sample for later *in situ* analyses.

(B) Annotated neuronal subtype from scVI[37] integration of 125 samples across five brain regions (Table S1) followed by clustering with Leiden algorithm, showing 20 discrete neuronal clusters (Table 1 and Figure S12).

(C) (Top) Nuclei counts for each detected neuronal subtype. Bar color indicates the brain region of origin for the nuclei comprising each subtype. (Bottom) Heatmap of neuronal subtype marker expression calculated from 2,000 random nuclei sampled from each subtype.

(D) (Top) Tau pathology as quantified by pT231/Total Tau ELISA across brain regions and stratified by Braak stage. (Bottom) Assessment of tau seeding activity across brain regions as measured by HEK seeding assay and stratified by Braak stage. Data are presented as mean ± SEM.

See also Figure S2; Tables S1, S8, and S11.

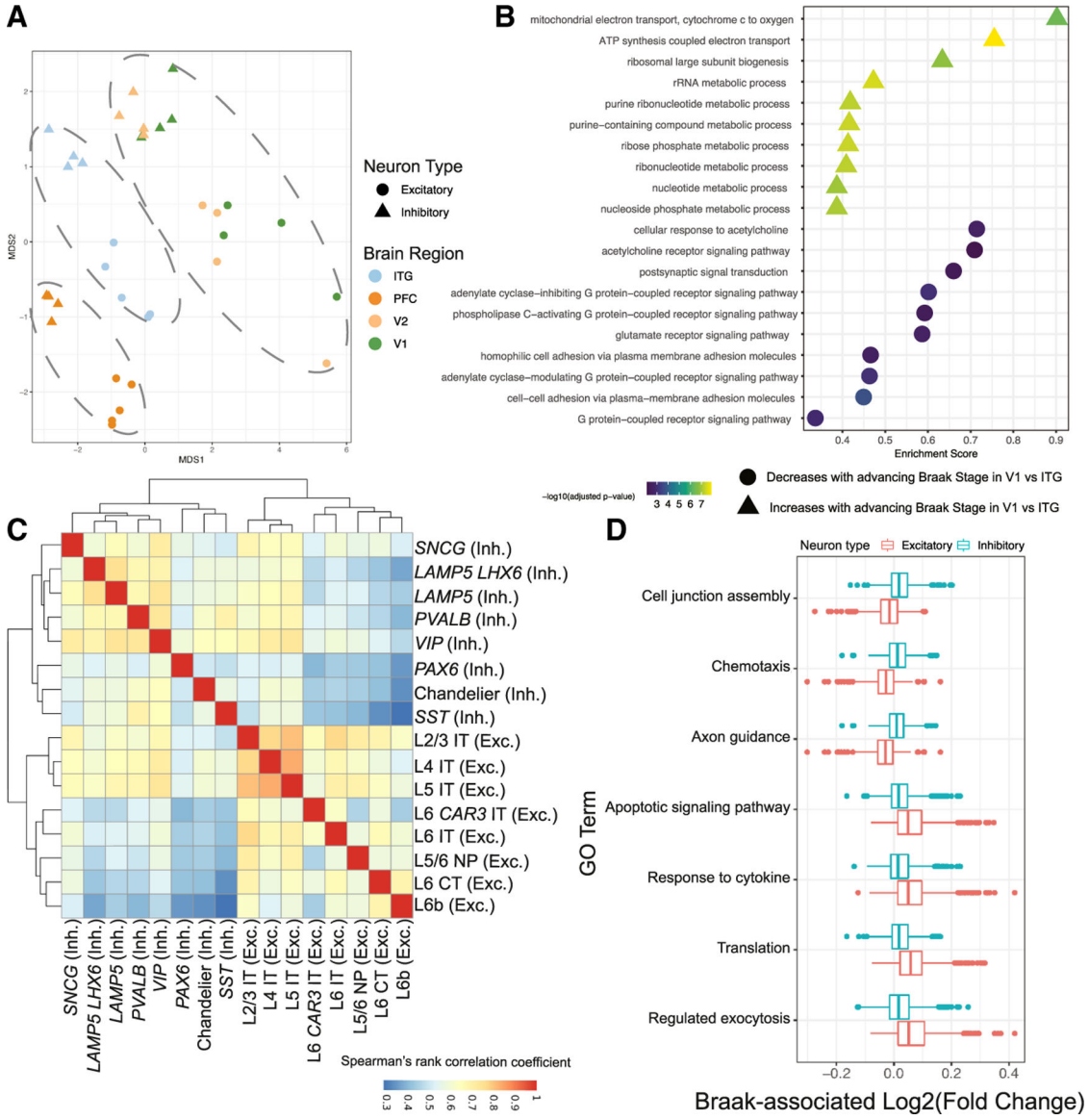

Figure 2. Transcriptomic changes associated with Braak stages

(A) Multidimensional scaling (MDS) plot based on the Braak associated $\log_2$(fold change) between each pair of samples from 14 neuronal subtypes and four brain regions (ITG, PFC, V2, and V1). Inhibitory (triangles) and excitatory (circles) subtypes are indicated by shape and brain region origin of subtype by color, and the ellipses show the grouping of the Braak-associated $\log_2$(fold change) by brain region.

(B) All GO terms that have significant −log10 (adjusted *p* value) differences with Braak-stage-associated gene-expression fold change between the ITG and V1. Colorbar denotes −log10 (adjusted *p* value).

(C) Heatmap showing pairwise correlation between Braak-associated fold changes in each neuron subtype from ITG. Rows and columns are clustered using ward.D2.[38] Inhibitory (Inh.) or excitatory (Exc.) status of the neurons is indicated next to each neuronal subtype label. Colorbar denotes Spearman's rank correlation coefficient.

(D) Boxplot showing difference in statistically significant ($p < 0.001$), Braak-associated $\log_2$(fold change) for selected enriched GO terms between inhibitory and excitatory neurons in ITG. Data are represented as mean ± SEM.

See also Figures S2 and S3; Tables S2, S3, and S10.

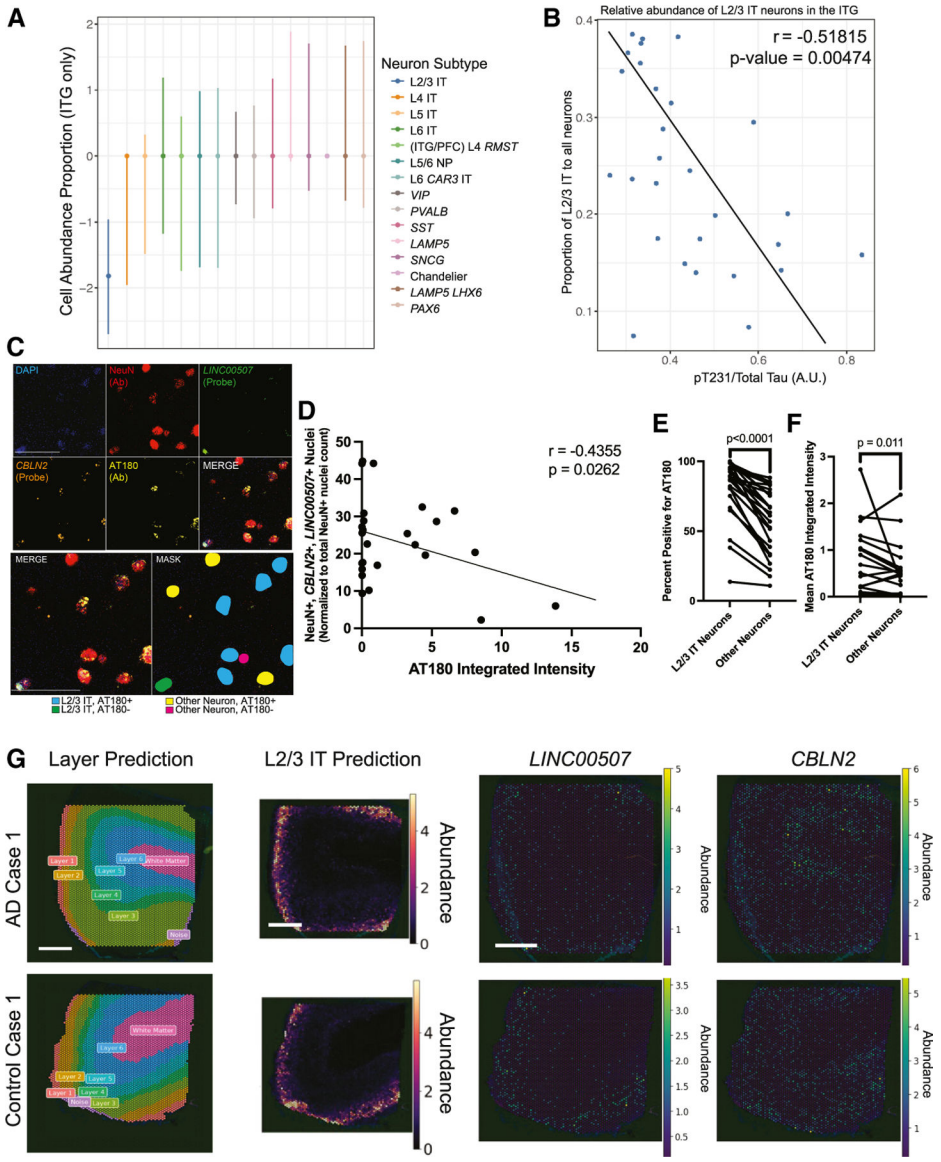

Figure 3. Transcriptomic and histological evidence of an association of L2/3 IT ITG neurons with pTau

(A) Dot-and-whisker plot showing the estimated pT231/Total Tau final parameter and 95% confidence interval derived from scCODA[39] analysis (STAR Methods) for each neuron subtype in ITG.

(B) Scatterplot showing the Pearson correlation (r = −0.51815, *p* value = 0.00474) of L2/3 IT neurons (number of L2/3 neurons/number of all neurons) with pT231 abundance for each sample in the ITG.

(C) Tau-vulnerable neurons (L2/3 IT neurons detected based on positivity of NeuN [antibody] and the number of copies of *LINC00507* [mRNA probe] and *CBLN2* [mRNA probe]) (STAR Methods). Tau pathology was measured by AT180 (pT231; antibody) immunopositivity within each detected neuronal cell body. Scale bars, 50 μm.

(D) Simple linear correlation (r = −0.4355, *p* value = 0.0262) of the abundance of L2/3 IT neurons and AT180 integrated intensity within the analyzed image area (STAR Methods).

(E and F) (E) AT180 integrated intensity of L2/3 IT neurons and all other neurons demonstrate that L2/3 IT neurons have higher probability of containing tau pathology (two-way Wilcoxon ranked pairs test, p value < 0.0001) and (F) present with significantly higher pTau burden compared to all other neurons on average (two-way Wilcoxon ranked pairs test, p value = 0.011).

(G) (Left) Spatial plot images from one AD and one control donor of medial temporal gyrus tissue with layer annotations derived from stereotypical cortical layer makers expressed in each spot (data from Chen et al.[40]; STAR Methods). Expected abundance of L2/3 IT neurons in each spot after cell-type annotation of spatial transcriptomics data to our annotation. The color bar depicts the abundance of L2/3 IT neurons in each spot. (Right) Expression of *CBLN2* and *LINC00507* transcripts in donor tissue sections. The color bar depicts abundance of transcripts in each spot. Scale bars, 1.3 mm.

See also Figures S1–S8 and Table S4.

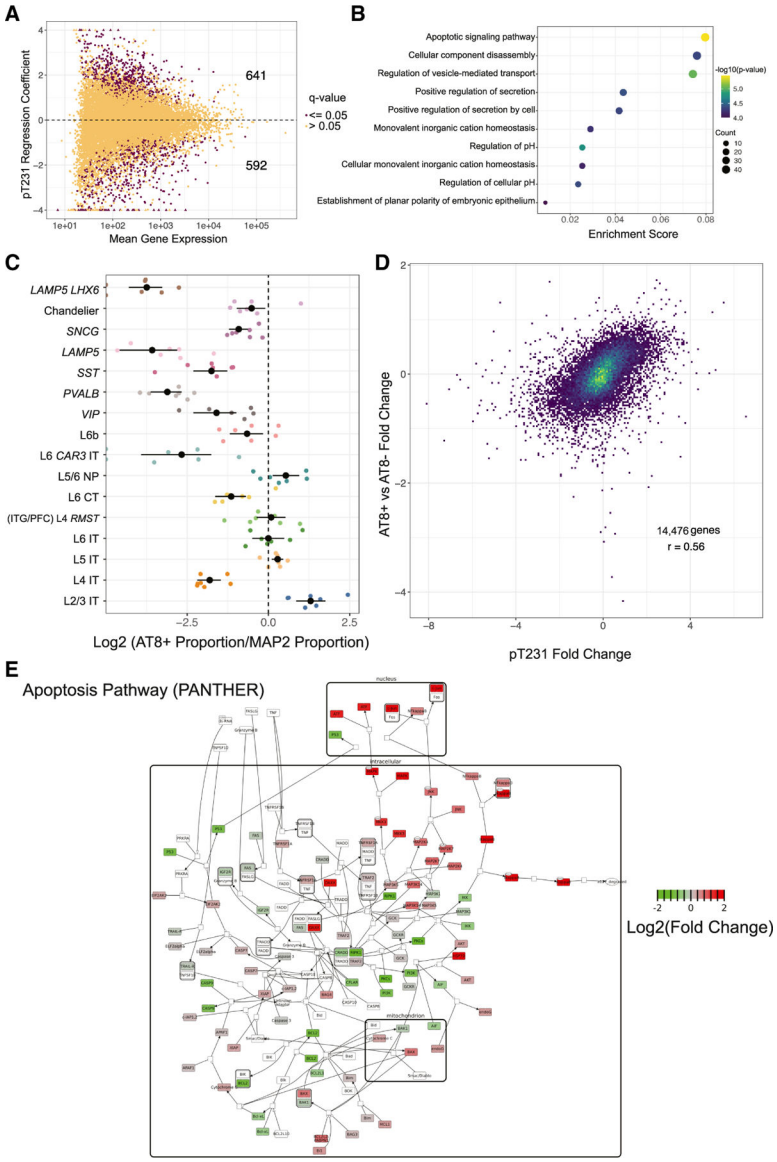

Figure 4. Transcriptional profiling of L2/3 IT neurons

(A) MA plot showing 641 genes with a significant positive pT231/Total Tau coefficient and 592 genes with significant negative pT231/Total Tau coefficient as identified in L2/3 IT neurons in ITG. Significance based on *q* value < 0.05, denoted in legend by color of data point.

(B) Dotplot showing −log10(*p* value) and enrichment score (number of genes in gene set/total number of differentially expressed genes) for top ten GO terms from an enrichment analysis of the 641 genes with a significant positive pT231/Total Tau coefficient. Colorbar denotes −log10(*p* value), size of data point denotes count.

(C) Dot-and-whisker plot showing the mean and 95% confidence interval of the log odds ratio of $AT8^+$ vs. $AT8^-$ neurons of each neuronal subtype in the Otero-Garcia et al.[12] dataset, based on our annotation. Log odds ratio is calculated for every sample as log(proportion of neuron subtype in $AT8^+$ fraction/proportion of neuron subtype in $AT8^-$ fraction).

(D) Density scatterplot of the $AT8^+$ vs. $AT8^-$ $\log_2$ (fold change) of L2/3 IT neurons in the Otero-Garcia et al.[12] dataset vs. pT231/Total Tau regression coefficient of L2/3 IT neurons in this study (r = 0.56). See also Figure S7.

(E) SBGNview[44,45] graphical representation of the apoptosis signaling pathway (PANTHER: P00006) from the PANTHER[46] database. Genes producing protein products in white boxes were not represented in L2/3 IT ITG neurons (percent expression <3%). Genes producing protein products in gray boxes held no association to pTau in L2/3 IT ITG neurons. Genes producing protein products in red boxes were positively associated and genes in green boxes negatively associated with pTau in L2/3 IT ITG neurons. Color bar denotes $\log_2$(fold change) (Table S4).

See also Figures S7, S9, S10, and S11; Tables S4, S5, and S7.

Table 1.

Identified neuronal subpopulations

Label	Marker gene 1	Marker gene 2	Marker gene 3	Marker gene 4	Primary brain region localization	Homogeneity	Primary cortical layer localization	Excitatory/ inhibitory
Chandelier	*SLC9A9*	*TMEM132C*	*CA8*	*ALK*	none	0.869167234	N/A	inhibitory
(EC) L2/3 *PALMD*	*PALMD*	*CNGB1*	*SEMA3D*	*SAMD3*	EC	0.754723804	2/3	excitatory
(ITG/PFC) L4 *RMST*	*RMST*	*PLCH1*	*OTOGL*	*AC073365.1*	ITG and PFC	0.918678977	4	excitatory
L2/3 IT	*CBLN2*	*TESPA1*	*AC013287.1*	*LINC00507*	none	0.975053045	2/3	excitatory
L4 IT	*SLC22A10*	*COBLL1*	*SLC38A11*	*AC073091.3*	none	0.894900593	4	excitatory
L5 IT	*LRRK1*	*AC016687.2*	*AC073091.3*	*HS3ST2*	none	0.777245509	5	excitatory
L5/6 IT	*HTR2C*	*NPSR1-AS1*	*GRM8*	*SORCS2*	none	0.977897954	5/6	excitatory
L6 CT	*SEMA3E*	*ADAMTSL1*	*MEIS2*	*SEMA3A*	none	0.81898054	6	excitatory
L6 IT	*THEMIS*	*CBLN2*	*AC019211.1*	*TESPA1*	none	0.782304354	6	excitatory
L6 *CAR3* IT	*POSTN*	*AC110023.1*	*NWD2*	*MAMDC2*	none	0.982900137	6	excitatory
L6b	*ZFHX3*	*PCSK5*	*LINC02232*	*ADAMTSL1*	none	0.898917855	6b	excitatory
LAMP5	*FBXL7*	*KIT*	*EGFR*	*AC132803.1*	none	0.933647686	N/A	inhibitory
LAMP5 LHX6	*PDGFD*	*CHST9*	*FBXL7*	*EYA4*	none	0.954871795	N/A	inhibitory
PAX6	*RELN*	*DDR2*	*CXCL14*	*NR2F2-AS1*	none	0.903326699	N/A	inhibitory
PVALB	*SOX6*	*BTBD11*	*MYO5B*	*TMEM132C*	none	0.869930151	N/A	inhibitory
SNCG	*CNR1*	*SGO1-AS1*	*NR2F2-AS1*	*ADRA1A*	none	0.833247334	N/A	inhibitory
SST	*SOX6*	*KIF26B*	*STXBP6*	*GRIK3*	none	0.973522725	N/A	inhibitory
(V1/2) L4 *LINC02055*	*LINC02055*	*AC008415.1*	*RYR3*	*EYA4*	V1 and V2	0.474143683	4	excitatory
(V1/2) L4 *TRPC3*	*LINC02388*	*TRPC3*	*VAV3*	*ARHGAP10*	V1 and V2	0.527291515	4	excitatory
VIP	*PROX1*	*DLX6-AS1*	*BTBD11*	*AC233296.1*	none	0.980354852	N/A	inhibitory

Description of the clusters visualized in Figure 1B. Clustering resolution was matched to a prior human transcriptomics study.[34] Determination of primary cortical layer localization was derived from the same study.[34]

KEY RESOURCES TABLE

REAGENT or RESOURCE	SOURCE	IDENTIFIER
Antibodies		
Mouse anti-3D6 antibody	AbbVie	Internally produced
Mouse anti-AT180 antibody	Thermo Fisher Scientific	Cat# MN1040; RRID: AB_223649
Mouse anti-NeuN antibody (Alexa Fluor 647)	Novus Biologicals	Cat# NBP1-92693AF647; RRID:AB_2927662
Mouse anti-OLIG2 antibody (Alexa Fluor 488)	Millipore Sigma	Cat# MABN50A4; RRID: AB_11205039
Rabbit anti-NeuN antibody	Abcam	Cat# ab236870; RRID: AB_2927651
Biological samples		
AD and control human brain samples	Neuropathology Core of the Massachusetts Alzheimer's Disease Research Center	N/A
Critical commercial assays		
BOND Polymer Refine Detection Kit	Leica	Cat# DS9800
Chromium Single Cell 3'Reagent Kit V3	10X Genomics	Cat# PN-1000075
MagMAX™ mirVana™ Total RNA Isolation Kit	Applied Biosystems	Cat# A27828
Phospho(Thr231)/Total Tau Kit	Meso Scale Diagnostics	Cat# K15121D
Precellys® CK14 Lysing Kit	Bertin	Cat# P000912-LYSK0-A.0
RNAscope® LS Multiplex Fluorescent Reagent Kit	ACDBio	Cat# 322800
Deposited data		
Raw sequencing data	This paper	BioProject: https://www.ncbi.nlm.nih.gov/bioproject/PRJNA1142727
Processed data	This paper	Zenodo: https://zenodo.org/records/13222113
Code	This paper	DOI: https://doi.org/10.5281/zenodo.13222113
Reanalysis of previously published datasets	Siletti et al.,[36] Otero-Garcia et al.,[12] Chen et al.,[40] Balusu et al.,[58] Mathys et al.[7]	Zenodo: https://zenodo.org/records/13222113
BICCN/Seattle AD Brain Cell Atlas reference medial temporal gyrus dataset	Jorstad et al.[34]	SEA-AD: NMhttps://sea-ad-single-cell-profiling.s3.amazonaws.com/MTG/RNAseq/Reference_MTG_RNAseq_final-nuclei.2022-06-07.h5ad
h5ad files	Siletti et al.[36]	CZ CELLxGENE: https://cellxgene.cziscience.com/collections/283d65eb-dd53-496d-adb7-7570c7caa443
Fastq files	Otero-Garcia et al.[12]	GEO: GSE129308
Visium (10X Genomics) spatial transcriptomics dataset of AD and control donors	Chen et al.[40]	GEO: GSE220442
Gene expression results	Balusu et al.[58]	DOI: https://doi.org/10.1126/science.abp9556
Differential gene expression results	Mathys et al.[7]	GitHub: https://github.com/mathyslab7/ROSMAP_snRNAseq_PFC/tree/main/Results/Differential_gene_expression_analysis.
Experimental models: Cell lines		

REAGENT or RESOURCE	SOURCE	IDENTIFIER
Human Embryonic Kidney Cells (Tau RD P301S FRET Biosensor)	ATCC	Cat# CRL-3275; RRID:CVCL_DA04
Software and algorithms		
Adobe Illustrator CC	Adobe	http://www.adobe.com/products/illustrator.html; RRID: SCR_010279
anndata	Virshup et al.[66]	https://scanpy.readthedocs.io/en/stable/generated/scanpy.tl.leiden.html
Cell2localization	Kleshchevnikov et al.[67]	https://github.com/BayraktarLab/cell2location
CellBender	Fleming et al.[68]	https://cellbender.readthedocs.io/en/latest/index.html
Cell Ranger v7.0.1	10X Genomics	https://support.10xgenomics.com/single-cell-gene-expression/software/pipelines/latest/installation; RRID: SCR_017344
clusterProfiler	Yu et al.[69]	https://www.rdocumentation.org/packages/clusterProfiler/versions/3.0.4
cmdscale	Venables and Ripley[70]	https://www.rdocumentation.org/packages/MASS/versions/7.3-61
cor	R.C. Team[38]	https://www.rdocumentation.org/packages/stats/versions/3.6.2
decontX	Yang et al.[71]	https://www.camplab.net/decontx/
DESeq2	Love et al.[72]	https://github.com/thelovelab/DESeq2
enrichGO	Yu et al.[69]	https://www.rdocumentation.org/packages/clusterProfiler/versions/3.0.4
GSEA	Broad Institute	http://software.broadinstitute.org/gsea/index.jsp; RRID:SCR_003119
HALO v.3.5.3577.173	Indica Labs	https://www.indicalab.com/halo/; RRID:SCR_018350
HALO FISH v2.2.0 module	Indica Labs	https://www.indicalab.com/halo/; RRID:SCR_018350
HALO ISH v3.4.8 module	Indica Labs	https://www.indicalab.com/halo/; RRID:SCR_018350
hclust	R.C. Team[38]	https://www.rdocumentation.org/packages/stats/versions/3.6.2
Leiden	Traag et al.[73]	https://scanpy.readthedocs.io/en/stable/generated/scanpy.tl.leiden.html
prcomp	Venables and Ripley,[70] Mardia et al.,[74] Becker et al.[75]	https://www.rdocumentation.org/packages/stats/versions/3.6.2
Prism 9	GraphPad	https://www.graphpad.com/scientific-software/prism/; RRID: SCR_002798
pyNNDescent	Dong et al.[76]	https://github.com/lmcinnes/pynndescent
qvalue	Storey et al.[77]	https://www.rdocumentation.org/packages/qvalue/versions/2.4.2/topics/qvalue
Rstudio Workbench 2021.09.2 + 382.pro1	Rstudio	https://docs.posit.co/ide/server-pro/2021.09.2+382.pro1/
Scanpy 1.9	Wolf et al.[78]	https://scanpy.readthedocs.io/en/stable/
pertpy	Wolf et al.[78]	https://pertpy.readthedocs.io/en/stable/
SBGNview	Dong et al.,[44] Luo and Brouwer[45]	https://github.com/datapplab/SBGNview
scDblFinder	Germain et al.[79]	https://rdrr.io/github/plger/scDblFinder/man/scDblFinder.html
scTransform	Hafemeister and Satija,[80] Choudhary and Satija[81]	https://cran.r-project.org/web/packages/sctransform/index.html

REAGENT or RESOURCE	SOURCE	IDENTIFIER
scVI	Lopez et al.[37]	https://docs.scvi-tools.org/en/stable/
Seurat v.3.1.3	Hao et al.,[82] Hao et al.,[83] Stuart et al.,[84] Bulter et al.,[85] Satija et al.[86]	https://www.rdocumentation.org/packages/Seurat/versions/3.1.4
stats (R)	R.C. Team[38]	https://www.rdocumentation.org/packages/stats/versions/3.6.2
ZEN software (Blue and Black)	Zeiss	https://www.zeiss.com/microscopy/us/products/software/zeiss-zen.html#zenversions; RRID: SCR_013672
Other		
Human *CBLN2* FISH probe, channel 2	ACDBio	Cat# 446058-C2; GenBank: NM_182511.4
Human *LINC00507* FISH probe, channel 1	ACDBio	Cat# 527218; GenBank: NR_046392.1
Bacillus subtilis DapB FISH probes, channel 1 & channel 2	ACDBio	Cat# 320758; GenBank: EF191515.1